

# Efficient surface defect detection in industrial screen printing with minimized labeling effort

Paul Josef Krassnig<sup>a,b,\*</sup>, Matthias Haselmann<sup>a</sup>, Michael Kremnitzer<sup>c</sup> and Dieter Paul Gruber<sup>a,b</sup>

<sup>a</sup>*Polymer Competence Center Leoben GmbH, Leoben, Austria*

<sup>b</sup>*Chair of Materials Science and Testing of Polymers, Montanuniversität Leoben, Leoben, Austria*

<sup>c</sup>*Burg Design GmbH, Steyr, Austria*

**Abstract.** As part of the evolving Industry 4.0 landscape, machine learning-based visual inspection plays a key role in enhancing production efficiency. Screen printing, a versatile and cost-effective manufacturing technique, is widely applied in industries like electronics, textiles, and automotive. However, the production of complex multilayered designs is error-prone, resulting in a variety of defect appearances and classes. These defects can be characterized as small in relation to large sample areas and weakly pronounced. Sufficient defect visualization and robust defect detection methods are essential to address these challenges, especially considering the permitted design variability. In this work, we present a novel automatic visual inspection system for surface defect detection on decorated foil plates. Customized optical modalities, integrated into a sequential inspection procedure, enable defect visualization of production-related defect classes. The introduced patch-wise defect detection methods, designed to leverage less labeled data, prove effective for industrial defect detection, meeting the given process requirements. In this context, we propose an industry-applicable and scalable data preprocessing workflow that minimizes the overall labeling effort while maintaining high detection performance, as known in supervised settings. Moreover, the presented methods, not relying on any labeled defective training data, outperformed a state-of-the-art unsupervised anomaly detection method in terms of defect detection performance and inference speed.

**Keywords:** Automatic visual inspection, surface defect detection, screen printing, machine learning, industrial anomaly detection

## 1. Introduction

Visual quality inspection plays a key role in achieving quality standards of premium manufacturers. As even the smallest defects in high-quality components lead to customer complaints, zero-defect policies are striven, resulting in visual inspection of every produced part. According to the manufacturing industry and the underlying production processes, manual visual inspection is still common. Therefore, huge amounts of human resources are required, conducting elaborate workflows accompanied with monotonous visual inspection tasks. This results in overlooked defects as well as unneces-

sary rejects of produced parts according to the subjective assessment of the operator [1]. In order to reduce these quality fluctuations and thus improve competitiveness, the automation of quality inspection processes as part of the emerging Industry 4.0 is mandatory [2, 3,4,5]. Thus, machine learning-based visual inspection systems [6,7,8] are intensively researched and build a crucial part for ensuring 100% fault-free products. High demand for automated visual inspection arises in the electronics industries [9]. Common inspected components include LEDs, semiconductor wafers and printed circuit boards [10]. In addition to electronics, there is high demand in the textile [11,12,13], printing [14,15,16] and automotive industries [17,18]. Automatic visual inspection systems can be applied to almost all materials such as polymers, metals, ceramics, glass, etc., regardless of the industry.

\*Corresponding author: Paul Josef Krassnig, Polymer Competence Center Leoben GmbH, Leoben, Austria. E-mail: paul.krassnig@pccl.at

### 1.1. Machine vision inspection process

In general, machine vision inspection can be roughly divided into three main stages: defect visualization, pre-processing, and inference. Based on the optical surface properties of the sample under investigation, appropriate optical components must be determined. These components include cameras (sensors incl. optics), illuminations, and filters, which are used to visualize defects and reduce the prominence of unimportant features. Thus, the objective of defect visualization is to maximize the contrast of imperfections on product surfaces in digital images, making them more easily identifiable and analyzable. Determining suitable optical components typically requires extensive laboratory experiments and domain knowledge. General approaches for automatically characterizing defect visibility, applicable to various surfaces and defect textures, remain an active area of research [19,20,21].

In addition to the common RGB and monochrome sensors in the visible range, sensors operating in the ultraviolet (UV) or infrared (IR) ranges can offer advantages for specific features. For instance, UV sensors (200–400 nm) reveal fine scratches on polished surfaces that are barely visible to the human eye (e.g. Sony's IMX487 [22]). Shortwave infrared (SWIR) sensors (900–1700 nm) are increasingly applied in the electronics and semiconductor industries to uncover subsurface defects [23]. Multi- or hyperspectral cameras, which combine different spectral bands (e.g. visible and IR), reveal spatial physical and chemical properties of the samples being examined [24,25]. These imaging techniques are particularly valuable in the food, waste management, packaging, agricultural, and pharmaceutical sectors [26,27]. However, exploiting additional spectral bands is accompanied by an increased workload for data processing. Besides the selected spectrum, the optimal optical modality is determined by the illumination conditions, including the illumination characteristics (e.g. direct, diffuse, structured) and its position relative to the surface and sensor (bright field, dark field or transmission).

In addition to the defect visualization capabilities, factors such as system integration complexity, data processing bandwidth and software interoperability, are crucial in selecting appropriate hardware for industrial applications.

Image preprocessing prepares the captured data for inference with the selected defect detection methods. This stage may involve tasks such as image registration, masking, resizing or data normalization, to name a few. Finally, inference is used for the decision-making, classifying the inspected product as normal or defective.

### 1.2. Industrial defect detection methods

With the rise of affordable computing power, deep learning-based research has gained significant momentum in machine vision tasks. Deep convolutional neural networks (DCNN) have shown superior performance over traditional defect detection methods that rely on manual feature engineering [28]. The performance of deep learning methods typically scales with the amount of available training data. However, collecting large quantities of labeled data is labor-intensive and often impractical for many industrial applications. In the context of surface defect inspection using supervised neural networks, this is a major limitation, as an extensive labeling process is required for each new product type to meet inspection standards. Consequently, current research focuses on semi- or unsupervised defect detection methods [29,30], which require minimal or no defective samples for training and are therefore of particular interest for industrial applications. By modeling the underlying data distribution of fault-free (normal) samples, unsupervised methods overcome possible generalization problems of supervised methods.

Since the publication of industrial defect detection datasets such as MVTec [31], several anomaly detection methods have emerged. These unsupervised methods can be broadly categorized into representation-based [32,33,34,35], generative model-based [36,37,38,39,40,41,42], and flow-based [43,44] approaches. Representation-based methods compare test data features with learned normal representations to measure feature similarity or distance. Flow-based methods map feature distributions to multivariate Gaussian distributions using normalizing flows, with deviations indicating anomalies. Both approaches use DCNN feature extractors pretrained on large datasets like ImageNet [45]. These methods are often memory and computationally intensive due to their architectures and algorithms, such as k-nearest neighbor. Furthermore, the feature extractors are biased towards the dataset used for pre-training, which leads to performance degradation in case of significantly different examined data distributions.

Generative models are designed to reconstruct normal data, failing to properly reconstruct defective regions resulting in anomaly scores. Despite progress with autoencoders [36], generative adversarial networks (GANs) [46,38,39] and denoising diffusion models [40,41,42], challenges persist in overcoming reconstruction limitations for fine-grained patterns as well as computational efficiency.

Additional approaches include synthesizing defective data samples for self-supervised pretraining or data

133 augmentation [47,48,49,50,51]. However, GAN-based  
134 synthetization tends to generate simple defect structures  
135 and struggles with complex patterns. In addition, these  
136 methods rely on large datasets including defective sam-  
137 ples for the initial training process. Recent research on  
138 few-shot generative models, including diffusion-based  
139 approaches, aims to address these issues [52,53,54,55].

140 Given the specific data distributions and detection  
141 tasks in industrial applications, specialized methods are  
142 crucial. The high permissible variability in complex  
143 design patterns of screen-printed products and their di-  
144 verse product portfolio demands robust and adaptable  
145 methods. In addition, short inference times are manda-  
146 tory in order to achieve the required process cycle times.

### 147 1.3. Related work

148 Ongoing research on defect detection of screen-  
149 printed products is being increasingly applied in the  
150 electronics industry. In Zhao et al. [56], the screen-print  
151 of batteries is inspected using a multi-level block tem-  
152 plate matching and k-nearest neighbor method. The pre-  
153 sented inspection system enables the detection of de-  
154 fects, such as blurred prints, local defects or scratches of  
155 the printed product logo, QR code and fabrication num-  
156 ber. Further work presents an automatic inspection sys-  
157 tem for surface defect detection of screen-printed mo-  
158 bile phone back glasses [57]. A dual brightfield imag-  
159 ing system is demonstrated for defect visualization. It  
160 consists of a coaxial bright field and a low angle bright  
161 field illumination, enabling the visualization of defects  
162 such as scratches, dents and discolorations. Defect de-  
163 tection was performed with a symmetric semantic seg-  
164 mentation network trained in a supervised manner. The  
165 training dataset consisted of 34 550 images (6742 de-  
166 fectives), achieving an average test precision and re-  
167 call of 91.8 and 95.3%. Another inspection solution for  
168 mobile phone cover glasses is presented in [58]. The  
169 system adopts backlight imaging in combination with  
170 a segmentation method trained in an adversarial man-  
171 ner utilizing a novel data generation process. A further  
172 defect detection method applied to a screen-printing  
173 process is based on an optimized U-Net++ [59] archi-  
174 tecture, which is described in [60]. To enable accurate  
175 detection of small defects in relation to the product size,  
176 only image patches were evaluated rather than the entire  
177 image. The visualization of the defects was done with a  
178 white backlight and a blue incident illumination. Using  
179 the patch-split method and a customized loss function,  
180 a dice score of 0.73 was achieved. Gafurov et al. [61]  
181 investigated smearing effects of screen-printed lines us-

182 ing deep neural networks (DNN) and CCD cameras,  
183 installed subsequent to the screen-printing process. For  
184 this purpose, a screen-printing mask was designed con-  
185 taining different line widths and spacings as well as  
186 a variation of squeegee directions. Using an adapted  
187 U-Net architecture, it was possible to detect smearing  
188 defects in various printing conditions.

189 Commercially available automatic visual inspection  
190 systems are known in the printing, glass and weaving  
191 industries [62,63,64,65,66,67,68,69,70]. However, in-  
192 spection solutions for defect detection in the field of  
193 screen-printing are rather limited. The company OMSO  
194 [71] offers a product for optical inspection of decora-  
195 tions on cylindrically shaped objects such as bottles,  
196 tubes and jars. Cugher's glass inspection system [72]  
197 enables the detection of defects on the screen-print de-  
198 signs of glass panels. Keko Equipment Ltd. [73] of-  
199 fers an automatic inspection system to inspect prints on  
200 multilayer green ceramic productions. The inspection  
201 software leverages e.g. golden template comparison ap-  
202 plicable for max. inspection areas of  $220 \times 220$  mm at  
203 a resolution of  $10 \mu\text{m}$ . An integrated inspection system  
204 following a screen-printing process is offered by Saku-  
205 rai Graphic Systems Corporation [74] by means of their  
206 SI Inspection Unit. Thereby, two line scan cameras in  
207 incident light illumination compare the screen-printed  
208 pattern to a master reference sample.

### 209 1.4. Contributions

210 The aforementioned studies and commercial auto-  
211 mated inspection systems mostly contain inspection so-  
212 lutions for printed product designs such as logos and  
213 labels, showing clearly defined geometries and image  
214 features. Due to non-complex print designs, e.g. by us-  
215 ing only a few print layers, the spectrum of possible de-  
216 fect causes and subsequent diverse defect appearances  
217 is reduced, which limits the effort of defect visualiza-  
218 tion. Frequently used deep learning-based segmentation  
219 models rely on pixel-wise labeled ground truth masks  
220 for supervised training and are therefore dependent on  
221 the amount and quality of labeled data.

222 The products studied for the given publication are  
223 designed for use as decorative patterns in a variety of  
224 applications, including products used in the automo-  
225 tive industry. In order to meet the customer's needs  
226 and requirements, complex designs are developed and  
227 manufactured under high quality standards. To achieve  
228 the desired visual impression of the decorative pattern,  
229 numerous manufacturing steps are necessary, result-  
230 ing in a complex multilayered design. Therefore, the

231 aim of this work was to develop an automatic visual  
232 inspection system that inspects decorated foil plates for  
233 production-related surface defects. Generally, the de-  
234 fects appear small in relation to the sample size being  
235 examined. The developed optical modalities must be  
236 able to display the different defect classes with suffi-  
237 cient contrast. Given the large product portfolio, the  
238 adaptability of the system to new product designs is of  
239 great importance. In addition, the applicability of auto-  
240 mated visual inspection in the production line should be  
241 ensured with regard to important process requirements  
242 such as cycle times. Due to the high labor involved in  
243 data acquisition and labeling, defect detection methods  
244 that provide sufficient detection performance with as  
245 little labeling effort as possible are emphasized. Fur-  
246 thermore, they must be capable of handling the allowed  
247 product to product variability.

248 Currently, there is no available inspection system for  
249 automated full-surface defect detection of decorated  
250 foil plates, accounting for allowed design and prod-  
251 uct variability and adaptability. It has to be mentioned  
252 that this publication builds upon the research work pre-  
253 sented at the ASPAI 2022 [75]. Optical modalities were  
254 introduced that enable the visualization of production-  
255 related defects with sufficient contrast. Therefore, labo-  
256 ratory experiments were conducted to analyze various  
257 design patterns of different products. The possible inte-  
258 gration of investigated optical modalities into the pro-  
259 duction line as part of an inspection approach was out-  
260 lined. By assigning the detected defect classes to the in-  
261 dividual production steps, deviations in the production  
262 process will be detected at an early stage.

263 Thus, the main contributions of this work can be  
264 summarized as follows:

- 265 – Investigation and application of developed optical  
266 modalities for sufficient defect visualization in a  
267 sequential inspection process, given production  
268 related requirements. This includes adaptability  
269 to different product sizes with a “field of view”  
270 (FOV) of up to 1200 mm, as well as to product  
271 designs with their various defect appearances and  
272 resulting defect classes.
- 273 – Introduction of scalable patch-wise defect detec-  
274 tion methods utilizing less labeled data, applicable  
275 for automatic full-surface defect detection. There-  
276 fore, a data preparation and preprocessing work-  
277 flow is presented, that minimizes the overall la-  
278 beling effort in supervised training settings, ap-  
279 plicable to various industrial manufacturing pro-  
280 cesses. This enables fast adaptability as allowable  
281 product-to-product variations and unseen defect  
282 types during production emerge.

- 283 – Development and implementation of an inspection  
284 system demonstrator in an industrial setting, capa-  
285 ble of automatic defect detection on decorated foil  
286 plates.

287 Section 2 illustrates the structure of decorated foil  
288 plates and briefly describes the manufacturing process.  
289 Frequently occurring defects are visualized and the for-  
290 mation process of selected ones is described. In Sec-  
291 tion 3 experimentally explored optical modalities are  
292 specified, followed by an introduction of the inspection  
293 system and its underlying procedures in Section 4. Sec-  
294 tion 5 presents the investigated defect detection meth-  
295 ods. Section 6 gives an evaluation of their defect detec-  
296 tion performance as well as inference speed and overall  
297 inspection time. Section 7 provides a summary of the  
298 key findings and an outlook for future improvements.

## 299 **2. Decorated foil plate**

300 The manufacturing process underlying the products  
301 studied is known as screen printing or silk screen print-  
302 ing. This is a cost-effective and versatile printing pro-  
303 cess that can be applied to a wide range of different  
304 materials such as textiles, metals, glass, wood and poly-  
305 mers [76]. The process is suitable for automation and is  
306 widely used in industries such as textiles, automotive  
307 and electronics [77]. Thereby, ink is deposited on the  
308 sample through a screen with a defined design. The  
309 screen consists of a frame with close-meshed fibers,  
310 forming a grid, onto which a UV-active photo emul-  
311 sion is evenly applied. Once the emulsion has dried, the  
312 desired design is transferred to the screen using a film  
313 exposed to a UV light source. Areas that have not been  
314 exposed to UV light are then washed out and are per-  
315 meable to the ink. In the subsequent printing process,  
316 the ink is transferred through the created stencil to the  
317 underlying sample. The sequential repetition of these  
318 production steps using separate screens for each ink  
319 layer enables the production of multilayer decorative  
320 patterns. The correct alignment of the individual layers  
321 to each other and the quality of each production step  
322 have an influence on the final print result.

323 Figure 1 schematically shows a typical structure of a  
324 decorated foil plate. Depending on the product design  
325 the dimensions of the carrier foil vary from A4 format  
326 to a width of 1200 mm. Typical materials are polymers  
327 such as polycarbonate (PC), poly(methyl methacry-  
328 late) (PMMA), acrylonitrile butadiene styrene (ABS),  
329 polyethylene terephthalate (PET) or polyvinyl chloride  
330 (PVC). The decorative pattern is formed by sequentially

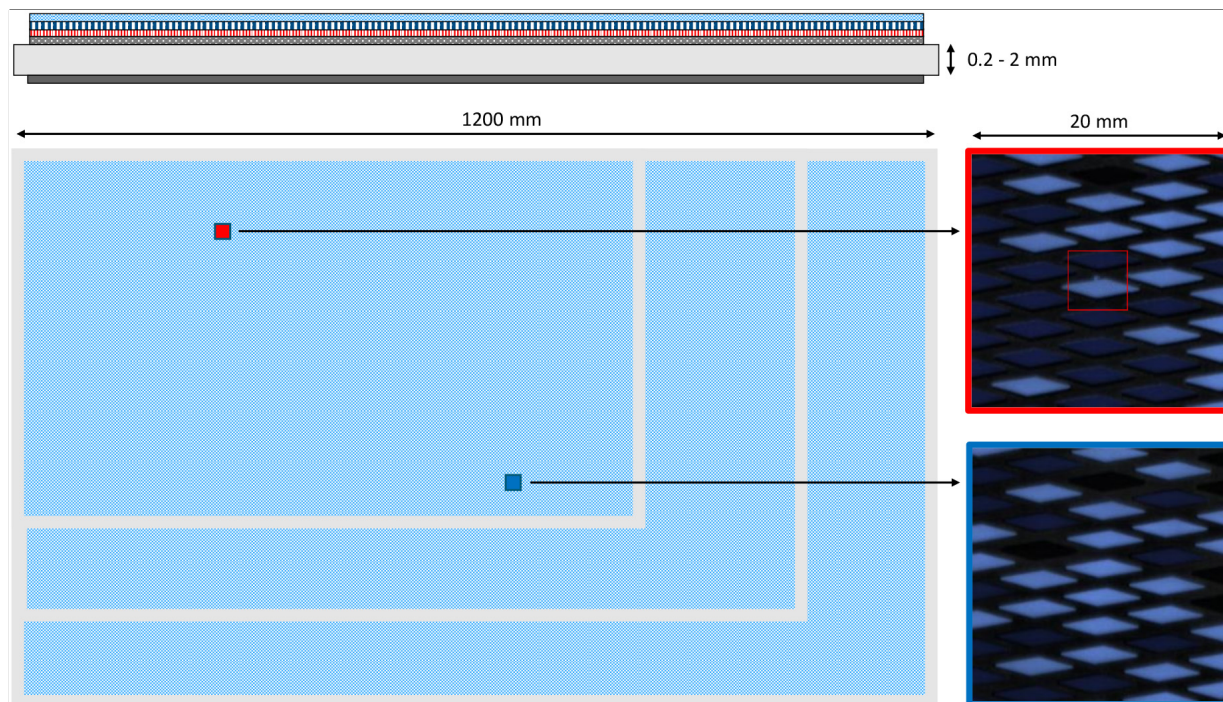


Fig. 1. Schematic multilayered design of a decorated foil plate showing possible defective (red) and fault-free patches (blue). Defects appear small (few pixels in extension) in relation to the investigated sample size of up to  $10^6$  mm<sup>2</sup>.

depositing ink layers on the front- and/or backside of the carrier foil. The customized screens determine the design as well as the possible print resolution, which is defined by the number of meshes per inch and the ratio of thread diameter to mesh opening [78]. Depending on the complexity of the decorative design, more than 10 different colored layers are applied. As a result, high-quality appealing decorative patterns are obtained, which in some applications can yield a visual 3D effect.

### 2.1. Defect formation process and defect classes

The complex manufacturing process results in a large number of possible defect causes. Basically, defects can occur in every manufacturing step, which cumulatively affect the final product. Understanding the origin of defects and their visual appearance is of central importance for optimizing the quality standards in the manufacturing processes and, in the event of their occurrence, for taking corrective action. In this work, possible process-related surface defects are investigated. In the case of surface defect detection, a defect can be generally described as any sufficient deviation from the normal sample, considering the allowable product variability. Typical defect classes include e.g. printing defects, inclusions, mechanical deformations, scratches,

smears, squeegee strokes, pinholes, dust and misregistered control markers. On the right side of Fig. 1, two image patches on a structured decorative pattern are illustrated. The defects appear small (approx. 0.07 mm<sup>2</sup> on the upper right defective patch), i.e. only a few pixels in size, relative to the product size of up to  $10^6$  mm<sup>2</sup>. A further characteristic is the high permissible design variability of the structured patterns. This is evident when comparing the variance in contrasts of the patches mentioned above. Depending on the location of occurrence and product design, these defects can also be defined as weakly contrasted.

Prior to each print cycle, the new print layer is precisely aligned to the existing layers. Any misalignment of individual print layers during this registration process will be visible in the printed pattern by a so-called pattern misalignment, which is apparent across the entire surface (Fig. 2, 1C/2C). Deviations during the ink application process, e.g. regions with too less ink application, lead to pinholes or inhomogeneities (Fig. 2, 2A/2B). Inhomogeneities are print layers with too low optical density and high variance in color values. Pinholes, in turn, appear as dot-shaped holes in the print pattern. Impermissible holes or closed meshes in the stencil of the screen can lead to screen and print defects (Fig. 2, 1B). Typical inclusions in individual ink layers, such as

331  
332  
333  
334  
335  
336  
337  
338  
339  
340  
341  
342  
343  
344  
345  
346  
347  
348  
349  
350  
351  
352  
353  
354

355  
356  
357  
358  
359  
360  
361  
362  
363  
364  
365  
366  
367  
368  
369  
370  
371  
372  
373  
374  
375  
376  
377  
378  
379  
380

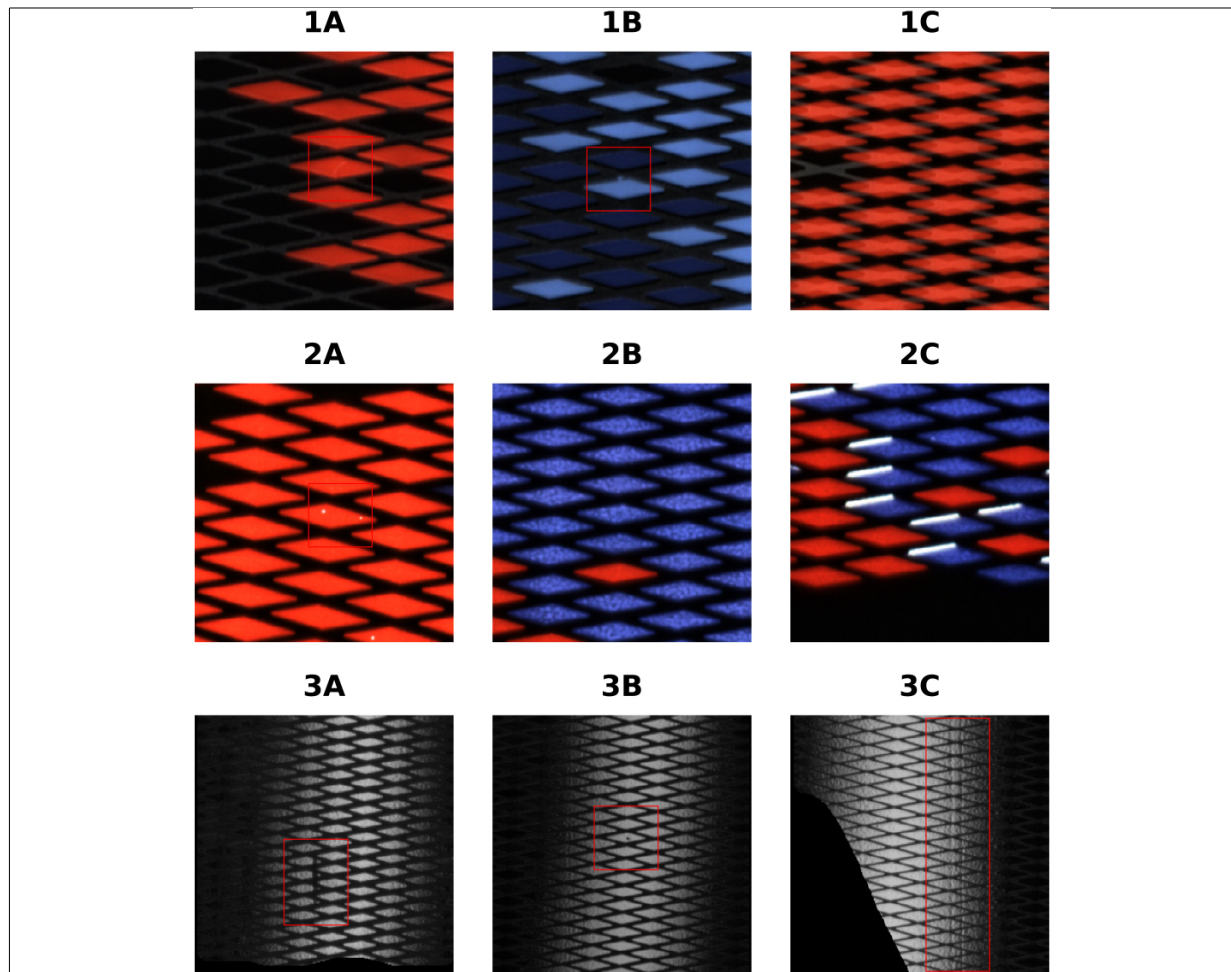


Fig. 2. Visualized defective patches of selected production-related defect classes captured by means of the customized optical modalities. Each row corresponds to a modality, from top to bottom: Line Scan Modality 1, Line Scan Modality 2, Area Scan Modality. Depending on their spatial appearance, defects can be divided into point defects such as inclusions (1A), screen or print defects (1B), scratches or dots (3A/3B) and pinholes (2A), or area defects such as pattern misalignment (1C/2C), inhomogeneities (2B) or squeegee strokes (3C).

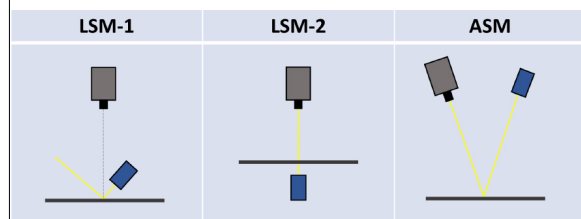


Fig. 3. Relative positioning of the camera sensors and illuminations regarding the utilized optical modalities: Line Scan Modality 1 (LSM-1), Line Scan Modality 2 (LSM-2) and Area Scan Modality (ASM), as presented at the ASPAI 2022 [75].

dust and fibers (Fig. 2, 1A), are caused by impurities in the process environment and electrostatic charge on the foil plates. Due to an electrostatic interaction with charged particles in certain inks, static splashes or stains

may also occur. Automatic or manual product handling can cause scratches or dots (Fig. 2, 3A/3B), as well as two-dimensional mechanical deformations, within the topcoat layer. Changes in the uniformity of the squeegee pressure and the dwell time of the ink on the screen can lead to a variable ink application. These so-called squeegee strokes (Fig. 2, 3C) are characterized as area defects and are affected by the printing direction.

### 3. Defect visualization

Defect visualization with sufficient contrast forms the basis of surface defect detection. Due to the characteristic design of decorated foil plates, a large number of defect classes emerge, which only become visible

381  
382  
383  
384

385  
386  
387  
388  
389  
390  
391  
392  
393  
394  
395  
396  
397

398 using certain optical modalities. In addition, some de-  
399 fect classes only occur in distinct decorative patterns.  
400 To find the best possible optical modalities, optical ex-  
401 periments were performed on a variety of decorative  
402 patterns and designs. According to the compliance stan-  
403 dards of the project partner, however, only images of a  
404 selected decorative pattern are illustrated in the given  
405 publication. The experiments included different sen-  
406 sor designs (area, line sensor) as well as illumination  
407 techniques (brightfield, darkfield, and transmission) in  
408 the visible range. As presented in [75] it turned out  
409 that three different optical modalities are necessary to  
410 visualize the wide range of defect classes. The optical  
411 modalities: Line Scan Modality 1 (LSM-1), Line Scan  
412 Modality 2 (LSM-2) and Area Scan Modality (ASM),  
413 consisting of camera and illumination as well as their  
414 positioning in relation to each other, are schematically  
415 visualized in Fig. 3.

### 416 3.1. Line scan modality 1

417 LSM-1 consists of an RGB linescan camera and a  
418 high intensity LED line bar (white, 6200 K). The il-  
419 lumination is equipped with a special lens and light  
420 amplifier foil to ensure the most directional and bright-  
421 est illumination in the focal zone. The optimum dis-  
422 tance, determined by the optical characteristics of the  
423 line bar, is approximately 50 mm above the sample's  
424 surface. The relative arrangement of light source and  
425 camera, enable a dark field illumination. The camera  
426 is placed planar to the sample's surface and the angle  
427 of incidence of the illumination is chosen as steep as  
428 possible w.r.t. the horizontal plane. This positioning  
429 avoids strong shadowing in complex decorative pat-  
430 terns showing a 3D effect. Patches 1A–1C in Fig. 2  
431 were recorded by means of this setup. Small punctual  
432 defects such as screen defects or inclusions that stand  
433 out only slightly from the background, are displayed  
434 in good contrast. Furthermore, area defects such as the  
435 pattern misalignment of an entire print layer, occurring  
436 as semitransparent white overlay in patch 1C, is clearly  
437 pronounced. This setup is applicable for defects affect-  
438 ing the decorated pattern like slurred prints. In addition,  
439 it addresses “sawtooth” defects, defined as continuous  
440 eroding at patterned edges, as well as misregistered  
441 control markers.

### 442 3.2. Line scan modality 2

443 LSM-2 similarly utilizes an RGB line scan camera  
444 and a high intensity LED line bar. The illumination is

445 placed planar and opposite to the camera aligned to  
446 its optical axis. As shown in Fig. 3, this setup allows  
447 transmission measurements of the investigated sample.  
448 As in LSM-1, the optimal distance is determined by  
449 the optical characteristics of the line bar (approx. 50  
450 mm behind the sample) to achieve the highest possible  
451 illumination intensity. A planar alignment of sensor and  
452 illumination to the sample's surface is mandatory to  
453 reliably investigate thicker layers on large-sized sam-  
454 ples, mitigating geometrical influences on the optical  
455 path. As in the LSM-1 setup, the camera distance is  
456 determined by the demanded maximum FOV as well as  
457 the required object pixel size and can be greater than  
458 1000 mm dependent on the sensor design. In addition  
459 to defects such as pinholes or pattern misalignment  
460 (Fig. 2, 2A/2C), it is also possible to display unwanted  
461 inhomogeneities in semitransparent colored print layers  
462 (Fig. 2, 2B). Line scan cameras in combination with  
463 high intensity line bars are generally the appropriate  
464 choice for the dynamic inspection of flat surfaces, as  
465 they are capable of capturing high resolution images at  
466 high measurement speeds, regardless of the sample size  
467 in the transport direction. However, the experiments  
468 conducted with the line scan camera revealed that the  
469 detection of defects on the transparent top layer was not  
470 satisfactory.

### 471 3.3. Area scan modality

472 To overcome above mentioned limitations an optical  
473 modality, consisting of an area scan camera and a light  
474 bar aligned in direct reflection, was designed (ASM  
475 in Fig. 3). Therefore, the LED light bar (white, 6200  
476 K) is placed as far away as possible from the speci-  
477 men's surface to create a large optical lever with re-  
478 spect to the monochromatic camera sensor. As shown  
479 in Fig. 2 3A–3C, this illumination method produces  
480 a bright area of direct reflection in the center, which  
481 decreases and fades out to the margins. Defects such as  
482 squeegee strokes or smears are only visible with high  
483 contrast in this transition area of reflection (Fig. 2, 3C).  
484 In general, bright-field images differ significantly from  
485 dark-field images in the LSM-1 and reveal defects in the  
486 transparent top layer, such as scratches and mechanical  
487 deformations (Fig. 2, 3A/3B). The majority of defects  
488 in the transparent top layer are only visible using this  
489 modality.

490 Utilizing all three modalities it was feasible to visu-  
491 alize the required production-related defect classes with  
492 sufficient contrast within the range of a few pixels in  
493 extension and minimum object pixel sizes of approx.

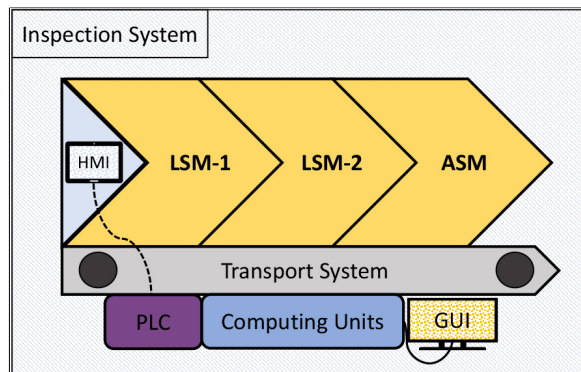


Fig. 4. Main components of the inspection system demonstrator, installed at the production site: Measurement chambers as LSM-1, LSM-2 and ASM; Programmable Logic Controller as PLC; Human Machine Interface as HMI; Graphical User Interface as GUI.

75  $\mu\text{m}$ . The different object pixel sizes are clearly apparent in Fig. 2, as patches 3A–3C map a larger FOV at the same pixel size ( $256 \times 256$  px) as patches 1A–2C captured by LSM-1 and LSM-2.

#### 4. Inspection system

The optical modalities enable a visualization of the production-specific defect classes with sufficient contrast. In order to perform an automatic visual product inspection using these modalities, an inspection system demonstrator was designed and installed at the project partner's production facility. The following main system requirements were considered: 1) Maximum product inspection time is determined by the conveyor speed and transport length and ranges between 15–30 s. 2) Product sizes of up to 1200 mm (FOV) should be examinable. 3) Adaptivity to different products and designs must be provided. 4) The defect detection methods must be able to detect smallest defects in relation to product sizes considering the allowed product to product variations. Furthermore, little efforts in data labeling as well as inference speeds applicable for in-line inspection are demanded.

##### 4.1. Inspection procedure

As shown in Fig. 4, the inspection system demonstrator consists of three measurement chambers, respectively one for each modality LSM-1, LSM-2 and ASM, which are arranged in sequence. Each measurement chamber is optically shielded to avoid both ambient light and unwanted reflections from different chambers. Regarding the above stated system requirements as well

as required optical modalities, suitable hardware components had to be selected. The hardware components of the measurement chamber LSM-1 and LSM-2 consist of commercial 16k RGB line scan cameras including optics and commercial high-power LED line bars according to Section 3. Due to the large required FOV of 1200 mm, 4 side by side monochrome area scan cameras (2.2 MP) incl. optics in combination with a high-power bar light are mounted in ASM. During each measurement cycle, the sample is manually placed on a conveyor belt and sequentially transported through all three measurement chambers. An installed rotary encoder generates trigger signals that enable distortion-free image acquisition at different conveyor speeds. Optical sensors detect the onset of the sample's surface and thus start image acquisition. Furthermore, the sensors characteristics were calibrated for a variety of decorated surfaces. The system parameters such as i.e. conveyor speed, illumination characteristics and sensor data are centrally controlled by means of a Programmable Logic Controller (PLC) and can be adjusted via an Human Machine Interface (HMI) panel. The inspection software operates on a distributed infrastructure. The computing unit consists of two computers, each with an NVIDIA GPU (GeForce RTX 2080 Ti resp. RTX 3090), a multicore processor and frame grabbers for the cameras.

##### 4.2. Data processing

The images of the LSM-1 and LSM-2 measurement chambers consist of  $16384 \times 12800$  px for each color channel at an FOV of 1200 mm in sensor direction. The images captured by ASM even contain  $8192 \times 65536$  px due to the image stitching procedure. This results in a data amount of 600 MiB per LSM-1 and LSM-2 chamber as well as 512 MiB in case of the ASM chamber. In total, approx. 1.7 GiB of image data are processed per measurement cycle. Given the required cycle times ranging from 15–30 s, this represents a major challenge in terms of data processing. For this purpose, a memory-optimized and parallelized data processing pipeline was developed. Thereby, the measurement data, starting from the raw image of the camera up to the final inference decision, are processed in parallel. Key processes include image acquisition, registration, segmentation, inferencing, post-processing and saving. A key feature of the data processing pipeline is that it avoids the evaluation of the entire image at once. Instead, as part of the preprocessing, overlapping image patches of size  $256 \times 256$  px are extracted



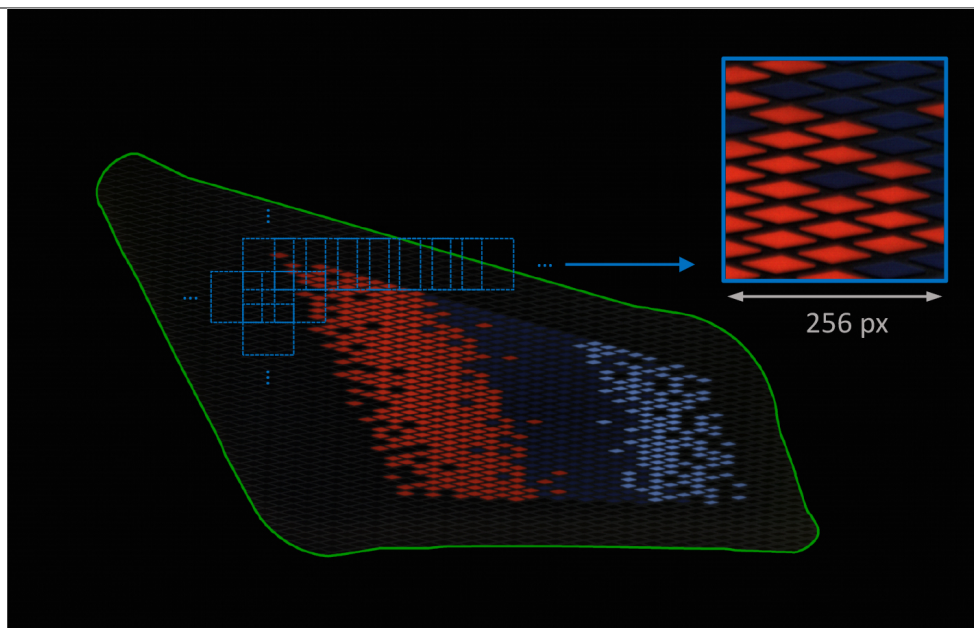


Fig. 5. Illustration of the patch extraction process in the defined ROI. Overlapping patches (blue squares) are extracted within the entire ROI-area (green), ensuring a minimum covered sample area at the borders.

573 within masked image regions that are relevant for de-  
 574 fect detection. This results in localized patch-wise de-  
 575 fect detection. As shown in Fig. 5, overlapping patches  
 576 (blue squares) are extracted in the so-called “region of  
 577 interests” or ROIs (green border) of the raw image in  
 578 the form of a grid covering the entire samples area.  
 579 These regions, predefined by domain experts, define  
 580 the product surfaces subject to inspection. A zoomed  
 581 fault-free patch is visualized in the upper right corner.  
 582 The overlapping patches with strides of 120–160 px  
 583 ensure that a potential defect is completely covered at  
 584 least in one patch, avoiding overlooking at borders. This  
 585 results in 170–300 patches per ROI. Depending on the  
 586 product size and the number of ROIs to be inspected,  
 587 there are several thousands of patches (e.g. 3400–6000  
 588 patches for 20 ROIs) to be evaluated per image and  
 589 measurement chamber.

#### 590 4.3. Calibration and image acquisition

591 The calibration of the measurement modalities in-  
 592 cluded optimizations of the rotary encoder settings,  
 593 photo responsive non-uniformity corrections, fixed pat-  
 594 tern noise corrections as well as white balancing. De-  
 595 pending on the modality, minimum exposure times of  
 596 100  $\mu$ s were selected to achieve the desired contrasts  
 597 and limit motion blurring. The MTF50 – value of LSM-  
 598 1 could be estimated with the help of an ISO Standard

12233:2000 calibration chart and a self-implemented  
 slanted edge method as described in [79] with 5 lp/mm.  
 With the help of the line scan cameras in the measure-  
 ment chambers LSM-1 and LSM-2, it was possible to  
 capture samples with FOVs of up to 1200 mm without  
 gaps. The acquisition of the entire FOV in measure-  
 ment chamber ASM is only possible by software stitch-  
 ing of the individual image frames. The difference of  
 LSM-1 and LSM-2 compared to ASM in the form of a  
 stretched geometry of the design, is evident in Fig. 6.  
 The frame rate was chosen as high as necessary (up to  
 40 frames per second) to avoid possible overlooking of  
 small defects in the aforementioned transition area of  
 direct reflection.

## 5. Defect detection methods

613  
 614 The characteristics of the surface defects to be de-  
 615 tected and the processing of large amounts of data  
 616 within the production related cycle times pose a chal-  
 617 lenge for the selection of suitable defect detection meth-  
 618 ods. The evaluation of thousands of patches, most of  
 619 which are fault-free, results in an imbalanced data dis-  
 620 tribution. In addition to a low false positive rate, de-  
 621 fect detection methods are required that exhibit suffi-  
 622 cient inference speed. In order to minimize the adapta-  
 623 tion effort per product, defect detection methods with

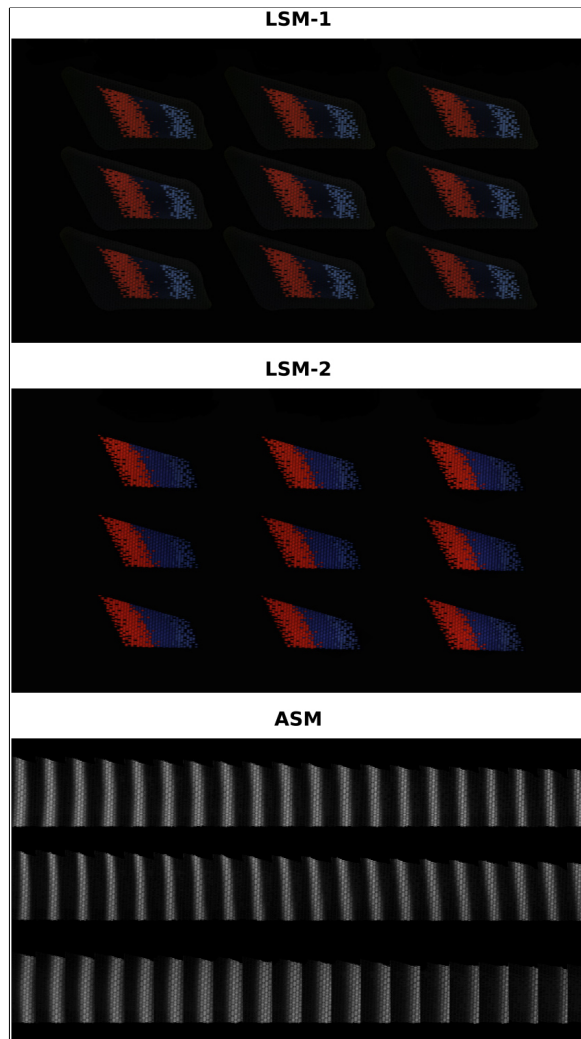


Fig. 6. Excerpts of masked sample images, acquired by means of the three measurement chambers: LSM-1, LSM-2 and ASM within a sequential run.

as little labeling effort as possible are preferred, while maintaining sufficient defect detection performance. The following section describes the defect detection methods utilized in each of the measurement chambers, as well as the data set preparation and method settings. As a baseline for benchmarking defect detection performance and inference speed, a state-of-the-art unsupervised anomaly detection method is introduced.

### 5.1. Supervised oversampling method

A widely used approach in machine learning to compensate for imbalanced data distributions are resampling techniques such as random undersampling or

oversampling [80,81]. In the case of an imbalanced data distribution of majority and minority classes, the samples from the respective class are randomly eliminated (undersampling) or copied (oversampling) to create a revised balanced dataset. In the course of this work, a scalable patch-wise oversampling method is introduced that enables efficient use of scarce and imbalanced data available. The following steps are necessary in providing fault-free (majority class) and defective data (minority class):

1. Masking of the individual ROI's of fault-free and defective samples and setting "out-of-ROI-values" to a integer value, e.g. zero.
2. Extraction of patches at random positions within the individual ROIs of the fault-free samples in the size of  $512 \times 512$  px, ensuring a minimum covered area between patch and ROI.
3. Augmentation of the extracted patches using random affine transformations (rotation, shearing, etc.) and random color transformations (brightness, contrast, etc.).
4. Centre cropping of 1/2 of the original patch size (height, width) to avoid image borders, caused by augmentation.
5. The resulting fault-free and augmented patches of size  $256 \times 256$  px are stored in a large file storage format, e.g. hdf5 or TSF as recently introduced in [82].
6. Extraction of defective patches of size  $512 \times 512$  px in the defective samples, ensuring central defect positioning within the patch.
7. Training of a (pretrained) DCNN in a supervised manner, whereby the defective patches are injected with a probability of 50% into the stream of fault-free patches. This step utilizes the same augmentation settings as described in 3, including center cropping ( $256 \times 256$  px).

Parameters such as the minimum ROI area covered per extracted patch and the maximum distance of random translations during augmentation, determined by defect type and patch size, must be carefully chosen. It is crucial to ensure that product surfaces are sufficiently represented and defects are covered after extraction and augmentation, to avoid e.g. generating defective patches that miss defective areas.

The samples used are pre-sorted by a domain expert prior to image acquisition, with separate samples for fault-free and defective data. This task eliminates any unwanted correlation between defective and fault-free patches in the subsequent data set generation. Thus, the labeling effort is limited only to the defective data at

known regions, since the extraction of fault-free patches is integrated into an automated process (step 1 to 5). Furthermore no elaborate pixelwise labeling of ground truths as in in segmentation based approaches is required. By extracting patches at random positions, the original dataset can be exploited as much as possible (several 100 000 patches from a few acquired images with large FOVs). Moreover, it is theoretically possible to collect an endless stream of fault-free patches. Another advantage of patch-wise evaluation is that the patch context focuses on image features that are relevant for defect detection, while ignoring unimportant ones. As with other supervised methods that use over-sampling techniques, attention must be given to possible overfitting. However, this method is easily scalable depending on data availability and thus can be fine-tuned as new defects emerge throughout the production process.

Above tasks can be seen as an applicable data-preparation as well as preprocessing workflow in industrial applications, reducing elaborate labeling only to known defective samples and sample regions.

### 5.2. Synthetic defect method

Another method used in this publication is based on the synthesis of artificial defects [48]. This algorithm enables the synthetization of defects with a wide range of appearances, imitating a large proportion of real occurring defects. Basically, the synthetization algorithm consists of four steps:

1. Generation of a binary defect skeleton, that is based on a stochastic process resembling a random walk with momentum.
2. Generation of a random defect texture, based on the previously generated binary defect skeleton.
3. Modification of the fault-free image patch by means of the randomly generated defect texture.
4. Assessment of defect visibility and rejection of synthesized defects below the visibility threshold.

By utilizing different sets of hyperparameters of the random variables used in steps 1–3, it is possible to generate a variety of different defect morphologies (straight, jagged, curved, circular skeletons, etc.) and characteristics (contrast, intensity distribution). Depending on the appearance of the real defects to be imitated (elongated, punctual as in Fig. 2), the hyperparameters that determine the distribution of the random variables must be chosen selectively.

Due to the transition region of direct reflection as well as the frequent occurring ROI borders, above de-

scribed method was adapted to generate visually apparent defects in both bright and dark contrasted areas, exclusively within the ROIs. Thus, defect synthetization categories and their underlying hyperparameters were adjusted based on real defects to produce bright and dark contrasted punctate and filamentous morphologies of different sizes and characteristics as depicted in Fig. 7. The preprocessing to generate the training and validation dataset follows almost the same procedure as steps 1–5 in Section 5.1. Additionally, following the central cropping in step 4, defects are generated in 50% of the fault-free patches. As a result, the generated training and validation datasets are balanced. With this method, it is therefore possible to perform balanced supervised training without the need for defective data. However, the generalization ability is only assessable using a test dataset containing real defects. Since the synthetization algorithm is based on grayscale, RGB images, if present, must either be converted or their channels processed independently.

### 5.3. Thresholding algorithm

LSM-2 enables the detection of pinholes, pattern misalignments or general inhomogeneities with low optical density. Due to the characteristics of the transmission measurement, defect features typically appear as white dots or areas of certain dimensions (Fig. 2, 2A/2C) within the image patch. To detect these features, a thresholding algorithm was developed, which is briefly described in the pseudo code of Algorithm 1.

The `connected_components()` function groups connected regions and assigns labels to the binarized image patches. These labels are then used to calculate the area of each defective region by counting the number of connected pixels per label. In order to utilize GPU-level parallelization the pseudo code shown in Algorithm 1 was implemented in a batchwise manner. With the help of this algorithm it is possible to tune parameters like RGB-thresholds and min. / max. defect areas, depending on the given quality requirements. As with other traditional image processing methods, no training data is demanded.

### 5.4. Baseline method

The representation-based method by Roth et.al [32], namely PatchCore, is based on the extraction of mid-level features of fault-free patches using a pre-trained DCNN. During the training phase, subsamples of these locally aware patch features are stored in a memory

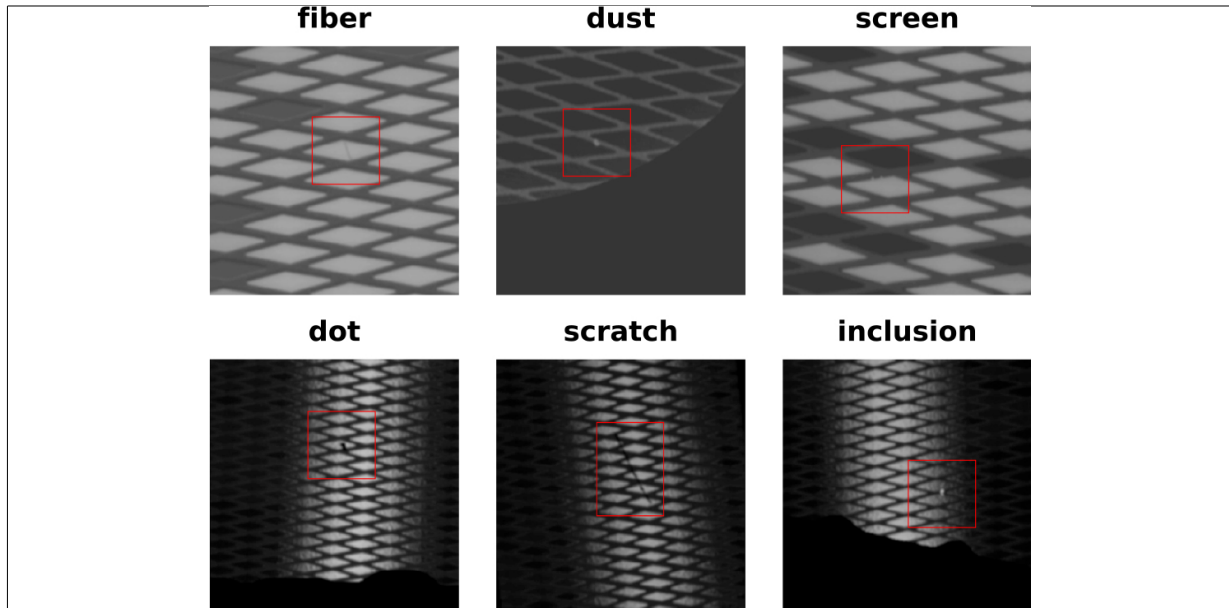


Fig. 7. Synthetic generated defects on fault-free patches of LSM-1 (top row) and ASM (bottom row). Hyperparameters were chosen to mimic punctual and elongated “real” defects as shown in Fig. 2.

783 bank. During inference, these features are compared  
 784 to the extracted features of the image using a near-  
 785 est neighbor search, resulting in anomaly scores. This  
 786 method achieves SOTA anomaly detection performance  
 787 on the MVTEC dataset, resulting in an image-level  
 788 AUROC of up to 99.6%.

### 789 5.5. Dataset and method settings

790 In order to evaluate methods described in section  
 791 5, image data were acquired by means of all three  
 792 measurement chambers (LSM-1, LSM-2, ASM) of the  
 793 inspection system demonstrator. Pre-sorted fault-free  
 794 samples as well as defective samples of different defect  
 795 classes were captured. The samples taken are in a state  
 796 in which the printing process, including drying, has al-  
 797 ready been completed. Therefore, defects that occurred  
 798 during printing are treated as fixed at this stage and no  
 799 further significant changes are expected. However, the  
 800 samples originate from different production batches and  
 801 therefore have a desirable permitted design variability.

802 A training, validation and test dataset was created  
 803 for each measurement modality. Each dataset consists  
 804 of patches cropped from the respective ROIs of the ac-  
 805 quired samples, resulting in an evaluation patch size of  
 806  $256 \times 256$  px. In order to avoid unwanted correlations  
 807 between the patches, the extraction of defective and  
 808 fault-free patches was done on separate samples. For  
 809 the same reason, fault-free and defective patches were

810 assigned to training, validation and test data from sep-  
 811 arate samples. This procedure allows for the creation  
 812 of uncorrelated datasets regarding defect classes and  
 813 data splits. The training data regarding the supervised  
 814 oversampling and supervised synthetic defect training  
 815 were created as described in section 5.1, by extracting  
 816 100 000 fault-free patches at random positions within  
 817 the ROIs. A total of 129 defective patches were col-  
 818 lected for the supervised oversampling training. The  
 819 extraction of overlapping fault-free patches for the cre-  
 820 ation of the training dataset for PatchCore, as well as  
 821 for the creation of the validation and test datasets, was  
 822 accomplished by using a sliding window with a stride  
 823 of 160 px. The LSM-1 dataset consists of 2014 and  
 824 1498 fault-free patches together with 74 and 95 de-  
 825 fective patches for validation and testing, respectively.  
 826 LSM-2 contains 406 and 393 fault-free as well as 44  
 827 and 110 defective patches for validation and testing.  
 828 The validation of the ASM was performed using a bal-  
 829 anced synthetic dataset as described in section 5.2, con-  
 830 taining 10 000 fault-free as well as 10 000 synthesized  
 831 defect patches. However, the test dataset contains 2060  
 832 fault-free and 74 “real” defective patches. In order to  
 833 imitate the slice wise image capture process in ASM,  
 834 the same defects may appear in different illumination  
 835 areas. In general, the datasets contain common defect  
 836 classes with respect to their optical modality, which  
 837 can be divided into point defects such as dust and fiber  
 838 inclusions, mechanical damages, print defects or pin-

839 holes, as well as area defects such as pattern misalign-  
 840 ment, punctual grid defects or squeegee strokes, etc.  
 841 (see Fig. 2). Furthermore, all different defect classes  
 842 are combined into one main defect class per modality.  
 843 As shown by the distribution of fault-free and defective  
 844 patches, imbalanced validation and test datasets were  
 845 created to mimic typical imbalanced inspection data  
 846 distributions.

---

**Algorithm 1:** Thresholding Algorithm
 

---

**Data:**

- Image Batch (batch\_size, channels, height, width)
- Threshold ( $r, g, b$ )
- Maximum pixel sum above threshold
- Minimum and maximum feature areas
- Filter kernel size ( $k$ )
- Image margin indices

**Result:**

- Predictions if patches are defective or fault-free
- Areas of connected components

```

1 for patch in batch do
2   for c in channels do
3     for i in {1, 2, ..., height} do
4       for j in {1, 2, ..., width} do
5         if i AND j in margins then
6           patch[c][i][j] ← 0;
7           continue;
8         if patch[c][i][j] ≤ threshold[c] then
9           patch[c][i][j] ← 0;
10        else
11          patch[c][i][j] ← 1;
12
13      if patch[r] AND patch[g] AND patch[b] = 1 then
14        binary_patch ← 1;
15      else
16        binary_patch ← 0;
17      dilated_patch ← dilation(binary_patch, k);
18      if 0 < sum(dilated_patch) ≤ px_sum_lim then
19        components ←
20          connected_components(dilated_patch);
21        for c in components do
22          areas ← component_areas(c);
23          if any area_lim_lower ≤ areas ≤
24             area_lim_upper then
25            predictions ← “defective”;
26          else
27            predictions ← “fault-free”;
28      else
29        predictions ← “fault-free”;
30
31 return predictions, areas;
  
```

---

### 5.5.1. Supervised oversampling/synthetic defect training settings

847 For both methods, network training was performed  
 848 using the stochastic gradient descent optimizer with  
 849 parameters (learning rate as  $5 \times 10^{-5}$  to  $10^{-4}$ , weight  
 850 decay as  $10^{-2}$ , momentum as 0.9) on a residual net-  
 851 work [83] namely ResNet18 pre-trained on ImageNet  
 852 [45]. Cosine annealing was used as the learning rate  
 853 scheduler, as described in [84]. As an additional pre-  
 854 processing step, the individual patches of the LSM-1  
 855 dataset were brightness-adjusted. In addition, a weak  
 856 smoothing was applied to all the modalities by using  
 857 a Gaussian kernel with a kernel size of 3 and a sigma  
 858 of 1. Mixed precision training was performed until sig-  
 859 nificant overfitting during validation occurred. In addi-  
 860 tion, models were selected based on the best Matthews  
 861 correlation coefficient (MCC) on the test data. Further-  
 862 more, thresholds for the underlying one-class classifi-  
 863 cation task were set according to the optimal F1-scores  
 864 obtained.

### 5.5.2. Thresholding algorithm settings

865 The thresholding algorithm (Algorithm 1) basically  
 866 contains a set of seven values out of four parameters  
 867 to be adjusted depending on the quality requirements  
 868 e.g. defect sizes. The three threshold values of the RGB  
 869 color channels, the min. and max. number of connected  
 870 pixels above the previously set threshold, and a filter  
 871 kernel size. The maximum pixel sum parameter is intro-  
 872 duced for reasons of computational speed. Furthermore,  
 873 it is possible to account for ignoring image margins  
 874 in strided patch-wise extraction scenarios. Threshold  
 875 values and other parameters were selected according to  
 876 the best detection performance based on a predefined  
 877 validation dataset as described in Section 5.5. There-  
 878 fore, the optimal parameters were chosen as follows:  
 879 Threshold RGB for all channels as 90 (uint8), min. and  
 880 max. defect area as 1 and 3000, the maximum pixel  
 881 sum as 15 000, the filter kernel size as 3. Patch margins  
 882 with a size of 40 px were ignored during inference.

### 5.5.3. Baseline settings: PatchCore

883 For reasons of adaptability, this paper investigates  
 884 a self-implemented version according to [32]. As fea-  
 885 ture extractor, layers 2 and 3 of a ResNet50 resp. wide  
 886 ResNet50 [85] pretrained on ImageNet were chosen  
 887 with a kernel size of 3 and stride of 1 used for average  
 888 pooling. IndexFlatL2 of the GPU-based Faiss library  
 889 [86] was selected for feature embedding, while omitting  
 890 coreset subsampling in order to exclude any defect de-  
 891 tection performance loss. For all datasets, all available  
 892 training patches were used for feature embedding, with  
 893 the upper limit set to 500 and the number of nearest  
 894 neighbors set to 3 resp. 5. Patch margins with a size  
 895 of 40 px were ignored during feature embedding and

evaluation of LSM-1 and LSM-2 to avoid common false positive detections in these areas. Furthermore, this is accompanied by an acceleration of inference speed. For LSM-1, an additional brightness adjustment was performed. As with the supervised methods above, the anomaly threshold for the binary classification task was chosen on the basis of the optimal F1-score. Prior to the experiments, the method was validated on the MVTEc dataset and resulted in an average image level AUROC of 98.5% for image sizes of  $256 \times 256$  px.

All methods were implemented in Python (version  $\geq 3.8.3$ ) using the GPU version of the PyTorch framework (version  $\geq 1.9.1$ ) with CUDA Toolkit version  $\geq 11.1.1$ . Experimental tests of the methods described above were performed on a NVIDIA GeForce RTX 3090, an AMD Ryzen 9 3950X 16-core processor and 64 GB DDR4 RAM running on OS Windows 10.

## 6. Method and inspection system evaluation

Experiments by means of the defect detection methods presented in Section 5 were conducted and evaluated regarding the patch-wise defect detection performance (Tables 1, 2) and the inference speed (Table 3). In addition, the overall inspection time of the implemented inspection system demonstrator was determined. As shown in Table 1, the defect detection performance is measured based on the entries in the confusion matrix, true negatives (TN), true positives (TP), false negatives (FN) and false positives (FP), and metrics obtained such as Matthews correlation coefficient (MCC) and false positive rate (FPR) as well as recall. Negatives correspond to fault-free patches, while positives represent defective ones. Commonly used metrics such as accuracy, F1-score or ROC-AUC are biased towards the majority class in the case of imbalanced data distributions. The MCC, with values ranging from  $-1$  (inverse prediction) to  $1$  (perfect prediction), includes all entries of the confusion matrix, thus making it an applicable metric eliminating the risk of overoptimistic outcomes [87]. Table 2 compares the methods used in LSM-1 and ASM in terms of their underlying defect group performance. Defect classes as in Fig. 2 can be broadly grouped into point or area defects, resulting in the imbalanced datasets as described in section 5.5. The defect detection methods are categorized according to their utilization of labeled defects. In contrast to the supervised oversampling method, PatchCore, the synthetic defect training and the thresholding algorithm do not rely on any labeled defective data for feature embedding or training.

### 6.1. Patch-wise defect detection performance

The following section provides a detailed analysis of the method's patch-wise defect detection performance, considering typical imbalanced inspection data distributions. The best performing method of each optical modality are highlighted in bold (Table 1). As in LSM-1, the supervised oversampling method achieved an MCC of 0.88 at an FPR of 0.2%, closely followed by synthetic defect training with an MCC of 0.85 and the same FPR. PatchCore resulted in a 6 times higher FPR and an MCC of 0.58. With the ASM setup, the best results were achieved through synthetic defect training with an MCC of 0.74 and an FPR of 0.5%. PatchCore performed even less well than in LSM-1, with an MCC of 0.26 and ten times higher FPR of 5.1%. In the absence of a sufficient number of defective samples, the supervised oversampling in ASM was skipped. Due to the clearly pronounced features in LSM-2, PatchCore performed robustly with an MCC of up to 0.95 and a comparatively low FPR of 0.8%. The thresholding algorithm presented in Algorithm 1 resulted in an MCC of 0.99 with only one overlooked defect.

Figure 8 shows the inference results by means of the PatchCore method including anomaly overlay. Rows 1–3 follow the optical modalities LSM-1, LSM-2 and ASM. Columns A–C are arranged according to TP, FN and FP classification. The image margins ignored during inference are clearly visible in 1A–2C. Large area defects, such as the grid defect in 1A, produced clearly pronounced areas of anomaly, whereas point defects, such as the print defect in 1B, were overlooked. The high allowable variance of the structured pattern, as shown in 1C, led to a large amount of false positive patches. Large distinct defects, such as the pattern misalignment in 2A and high contrasted pinholes, produced large deviating feature vectors with respect to the learned feature embedding, leading to proper defect detection. However, small and low contrasted pinholes as illustrated in 2B were more likely to be missed. As with LSM-1, small feature variations in the vicinity of masked border regions also led to anomaly scores, resulting in false positives as in 2C. The ASM dataset poses a challenge regarding defect detection due to its high contrast variance in the transition region of direct reflection and its frequently appearing masked ROI regions. As shown in patches 3A and 3C, many false positives occurred at the border areas of the ROI as well as in before mentioned transition regions. Possible imperfect ROI segmentation also introduced additional feature variance, leading to false positives. Frequently,

Table 1  
Patch-wise defect detection performance metrics of leveraged methods; supervised oversampling method (Oversampling), synthetic defect method (Synthetic Defects), threshold algorithm and the baseline method PatchCore. The test datasets are imbalanced to mimic typical inspection data distributions that overrepresent fault-free samples. The best performing method of each optical modality are highlighted in bold

Modality	Method	#Real defects	TN	TP	FN	FP	MCC	Recall (%)	FPR (%)
LSM-1	Oversampling	42	1493	69	26	5	0.81	72.6	0.3
		129	1495	77	18	3	<b>0.88</b>	81.1	0.2
	Synthetic defects	0	1495	72	23	3	0.85	75.8	0.2
	PatchCore	0	1478	49	46	20	0.58	51.6	1.3
LSM-2	Thresholding	0	393	109	1	0	<b>0.99</b>	99.1	0.0
	PatchCore	0	390	104	6	3	0.95	94.5	0.8
ASM	Synthetic defects	0	2049	50	24	11	<b>0.74</b>	67.6	0.5
	PatchCore	0	1954	29	45	106	0.26	39.2	5.1

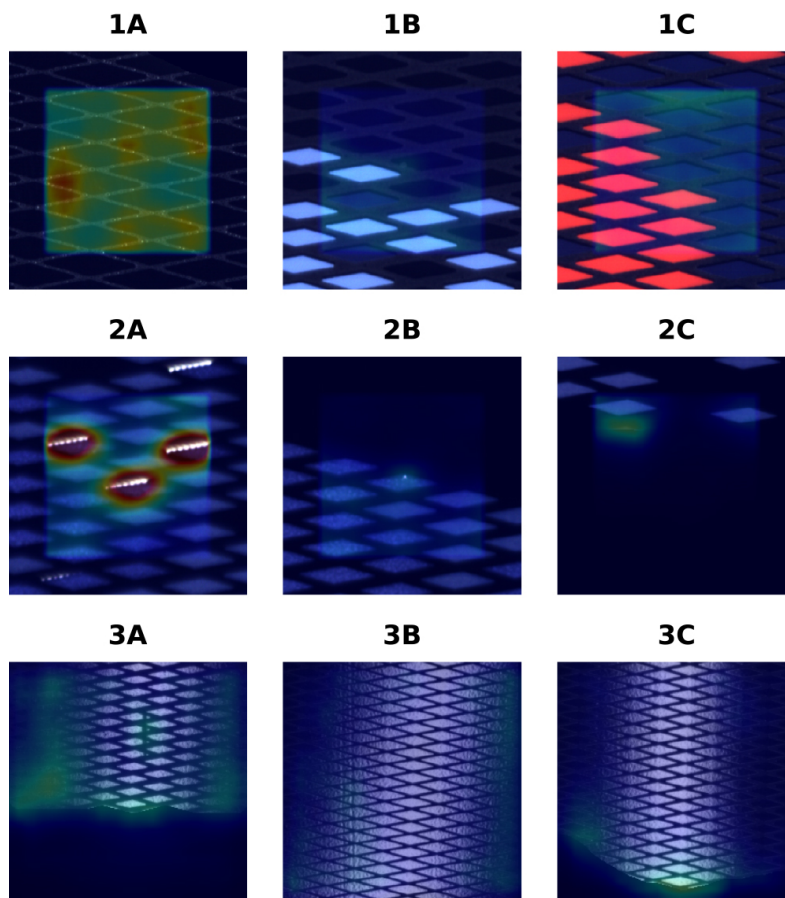


Fig. 8. TP, FN and FP (columns) patch inference results of LSM-1, LSM-2 and ASM (rows) using PatchCore. Large area defects, such as the grid defect in 1A as well as the pattern misalignment in 2A produced clearly pronounced areas of anomaly. However, small and weakly contrasted point defects, such as the print defect and the pinhole (1B/2B), were overlooked. Feature variations in the vicinity of masked border regions (2C/3C) and transition regions of direct reflexion (3A) introduced many false positives.

999 TP patches were classified as defective because of these  
1000 detected regions, whereas large area defects such as  
1001 squeegee strokes in 3B were partially or not detected at  
1002 all.

1003 Table 2 illustrates the performance metrics obtained  
1004 by means of the oversampling and synthetic defect

1005 methods in LSM-1 and ASM. For this purpose, the met-  
1006 rics previously shown in Table 1 were divided into their  
1007 individual defect groups, point and area. In case of the  
1008 supervised oversampling method in LSM-1, no area  
1009 defect was overlooked, resulting in a recall of 100%.  
1010 By utilizing synthetically generated defects as visual-

Table 2

Patch-wise defect detection performance metrics comparing the methods supervised oversampling (Oversampling) and defect synthetization (Synthetic Defects) by means of the defect groups Area and Points. The test datasets are imbalanced to mimic typical inspection data distributions that overrepresent fault-free samples. The best performing method of each Defect Group are highlighted in bold

Modality	Defect group	Method	TN	TP	FN	FP	MCC	Recall (%)
LSM-1	Area	Oversampling	1498	49	0	3	<b>0.97</b>	100.0
		Synthetic detects	1495	42	7	3	0.89	85.7
ASM			2049	14	19	11	0.48	42.4
LSM-1	Points	Oversampling	1495	28	18	3	0.74	60.9
		Synthetic detects	1495	30	16	3	0.76	65.2
ASM			2051	36	5	11	<b>0.82</b>	87.8

ized in Fig. 7, a recall of 86% was obtained. Overall, area defects have not been synthesized and their morphology is completely different with respect to their optical modality in LSM-1 and ASM. This can be observed in Fig. 8, comparing the grid defect in 1A with the squeegee stroke defect in 3B. The grid defect contains punctate features, comparable to some synthesized point defects in LSM-1, thus potentially led to a robust recall of the above described 86%. The synthetic defect method performed slightly better than the supervised oversampling method in detecting point defects, resulting in a recall of 65%. In general, the detection of small sized defects in this modality is challenging, due to their weak appearance in surrounded structured patterns (Fig. 2 1A).

However, in the case of ASM, the detection of point defects was superior to LSM-1 with a recall of 88%. Although the morphology of the synthesized defects in ASM is completely different from that of area defects (as shown in Fig. 2, 3C), this defect group achieved a recall of 42%. This can be seen as the ability to learn the underlying distribution of the fault-free data using the influence of the vast amounts of augmented fault-free and synthetic defect patches.

Furthermore, the low FPR of 0.2–0.5% observed with these supervised learning procedures, with respect to the remaining high recall of certain defect groups, indicates strong generalization ability. Another indicator of its robustness is that possible imperfect ROI segmentations, such as those seen in ASM (e.g. holes within darkly contrasted ROI regions), which lead to false positives in PatchCore, are not noticeable during inference utilizing the synthetic defect method.

As shown in Table 1, the supervised oversampling method achieved an MCC of 0.81 and an FPR of 0.3% by leveraging a reduced set of 42 labeled defects. This gives an indication of the scalability of this method when compared to the metrics obtained using 129 labeled defects. As stated above 170–300 patches per ROI are evaluated, thus to avoid any false alarms FPR

less than 0.59 resp. 0.33% are required to be applicable for inspection runs. Despite PatchCore, struggling with high FPR, introduced methods are capable of achieving even lower FPR.

## 6.2. Inspection speed

In addition to the evaluation of defect detection performance, the inference speed of the applied defect detection methods was determined. As shown in Table 3, the inference times and their reciprocal, the throughput of patches per second, were measured in combination with their CUDA memory footprint. According to the image processing pipeline as described in Section 4.2, image batches with batch sizes of 128 were chosen for evaluation. However, in the case of PatchCore, the batch size was reduced to one. The use of large feature embeddings of 1.5 and 3.1 GiB resulted in a high computational GPU utilization of up to 91%, preventing any noticeable speed-up by means of larger batch sizes. The test image batches consisted of either dummy data sampled from a uniform distribution, or selected defective and fault-free patches yielding to torch tensors (float32) allocated on the GPU.

The performance measures shown in Table 3 were determined using the arithmetic mean of 5 cycles with 100 repetitions, including preprocessing of the respective methods. Prior to each measurement cycles, a GPU warm-up of 10 repetitions was performed. To account for asynchronous CUDA data processing, inference times were measured using PyTorch's synchronized CUDA events [88]. The GPU memory footprint of each method was determined using `torch.cuda.mem_get_info()`, deducting PyTorch's CUDA context of approximately 1.3 GiB.

As expected, the ResNet18 architecture, used by means of the supervised oversampling and the synthetic defect method, achieved the lowest inference time of 0.18 ms, resulting in a throughput of 5556 patches/s. Inference times larger than 1000 patches/s have already



Table 3

Patch-wise inference speed measurements of utilized methods resp. their underlying architectures; supervised oversampling method and synthetic defect method (ResNet18), thresholding algorithm and the baseline method PatchCore

Method	Data	Margin px	Inference time ms	Throughput patches/s $\pm$ std	Memory-Footprint GiB
Thresholding	Dummy	0	1.81	$552 \pm 3$	1.2
		40	1.18	$847 \pm 5$	
	Defective Fault-free	40	1.13	$885 \pm 6$	
		0	0.58	$1724 \pm 1$	
PatchCore	Defective	0	118.89	$8 \pm <1$	6.0
	Defective	40	32.95	$30 \pm <1$	4.5
ResNet18	Dummy	0	0.18	$5556 \pm 9$	2.3

been reported for ResNet architectures in [89]. The dependence of the threshold algorithm on the input data is clearly visible in Table 3. The highest inference time was measured with 1.81 ms in the case of the dummy data and 0.58 ms for fault-free data, missing defective pixels and thus skipping the computation of defective areas. These values represent the estimated upper and lower bounds. Thus, in an industrial setting with a majority of fault-free patches per batch, throughputs of up to 1724 patches/s can be achieved. Due to the exhaustive nearest neighbor search in large feature embeddings, PatchCore led to by far the highest inference times of 32.95 and 118.89 ms. This means that both the thresholding algorithm and the methods that utilize the ResNet18 are approx. 57–183 times faster compared to the PatchCore configuration, that ignores image margins. Although, ignoring image margins for feature embedding and subsequent feature comparison led to a approx. 3.6 times reduction in inference time. For comparison, a thorough evaluation of SOTA anomaly detection methods inference speeds, including PatchCore, can be explored on p. 21 in [35]. The proposed method, namely EfficientAD, achieved the highest throughput of up to 614 patches/s, including CPU to GPU transfers. Thus, in inspection settings described above, embedding-based methods like PatchCore would lead to bottleneck the overall inspection process, not achieving required cycle times. In terms of memory footprint, the thresholding algorithm exhibits the smallest value with 1.2 GiB, followed by ResNet18 with 2.3 GiB and PatchCore with up to 6.0 GiB.

### 6.3. Inspection system demonstrator performance

The inference times determined above do not include all data processing steps during defect inspection as described in Section 4.2, such as registration, ROI segmentation or patch extraction, etc. To account for these computationally intensive tasks and to estimate

the overall inspection time of the implemented inspection system demonstrator, separate runs of the samples through all measurement chambers were performed. The best performing methods regarding defect detection performance (bold in Table 1) were therefore chosen for each modality. The time measurements started at the onset of image acquisition in LSM-1 and ended after finishing the post-processing of all modalities to ensure the availability of patch-wise inference results. A total of 10 inspection runs with various samples resulted in an average inspection time of  $20.25 \pm 0.59$  s, thus achieving the required cycle time range of 15–30 s. It has to be mentioned that the estimated overall inspection time is generally dependent on the product size and the resulting amount of evaluated patches as well as method settings. As with other hardware-dependent measurements, speed up leveraging more performant e.g. GPUs can be expected.

In terms of defect detection performance, it was qualitatively observed that the used defect detection methods are capable of detecting the wide range of different defect classes with high sensitivity at low false positive rates, confirming the metrics in Table 1. In the case of LSM-1, small defects that differ only slightly from their surroundings are more likely to be overlooked than area defects that are pronounced over the entire ROI. Despite the observation of missed defects (mostly area defects) in the test dataset of ASM resulting in a relatively low MCC of 0.74 compared to other modalities, this was not the case when performing inspection. Due to the high frame rates in ASM, the possibility of a defect occurring in more than one patch as well as in different illumination regions is increased and thus counteracts the determined dataset-specific recall. However, a thorough quantitative evaluation of the system's defect detection performance, considering the quality standards of the project partner, should be carried out in the future.

## 7. Conclusions and outlook

This work presents a novel automatic visual inspection system for decorated foil plates, applicable for full-surface defect detection. Developed optical modalities embedded in a sequential inspection procedure, enable defect visualization of production related defect classes with sufficient contrast. Thereby, applicability and adaptability to various product sizes with FOV's of up to 1200 mm as well as different product designs is ensured. Introduced patch-wise defect detection methods namely, supervised oversampling-, synthetic defect method as well as the thresholding algorithm are applicable for full-surface defect detection of small defects (few px in extension) in relation to large sized samples of up to  $10^6$  mm<sup>2</sup>. Therefore, defect detection performance and inference speeds considering inspection related requirements such as e.g. FPR and cycle times were determined. The synthetic defect method as well as the thresholding algorithm do not rely on any labeled defective training data. By means of these methods it was possible to achieve MCC's of up to 0.85 resp. 0.99, thus outperforming SOTA unsupervised anomaly detection method PatchCore. The obtained metrics of the synthetic defect method underline their applicability on structured patterns, although the determination of suitable hyperparameters is time-consuming. Its automatization would be beneficial for increasing further usability.

In terms of defect inspection, area defects that are pronounced over large sample areas are statistically more likely to be detected by patch-wise inference than the less sampled point defects. Additionally, area defects are more apparent than weakly pronounced point defects in terms of defect visualization. Furthermore, area defects, such as pattern misalignments, generate numerous defective patches per sample that can be used for subsequent training. Thus, point defects are more relevant to defect synthesis as they are easier to overlook and more sparse.

Furthermore, an industry-applicable data preprocessing workflow has been introduced, minimizing the labeling effort in supervised settings. This workflow leverages the automatic extraction of patches from pre-selected fault-free samples, eliminating the need for exhaustive screening of thousands of patches. Overlooked defects, such as potential process contamination, had no significant impact on the training process. This is likely due to the extraction of a large number of patches (100 000) and the clean sample preparation by domain experts. Thus, manual labeling is limited to the extrac-

tion of defective patches at known positions on separate defective samples. This scalable balanced learning procedure is able to achieve the demanded FPR as well as recall, due to the possible utilization of available fault-free resp. defective samples during production. The proposed workflow is not limited to screen-printed products with flat surfaces. Tests on 3D-shaped products using additional viewpoints indicated its applicability to various industrial manufacturing processes (e.g. injection molding, forging, additive manufacturing), minimizing the overall labeling effort.

Defect detection of small and weakly pronounced defects in its underlying structured patterns remain challenging as in case of point defects in LSM-1. Optimization in recall could be obtained by separately training of area and point defect groups, assuming sufficient defective data is available for each class. Additionally, subsequent classification of individual defect classes would be possible enabling logging of defects statistics. Exploiting fault-free data of all modalities and performing a self-supervised pretext task (e.g. with synthetic defects) would generate a robust feature extractor, applicable for subsequent fine-tuning with collected defective samples on same or similar patterns. Furthermore, including available defective data samples during synthetic defect training as presented in [90] would be another viable strategy in improving detection performance.

Regarding the thresholding algorithm, attention has to be given to product designs with low optical density, introducing possible false alarms. One strategy could be appropriate masking ignoring these specific regions. In case of defect visualization in ASM, one has to keep in mind that orientation dependent defect classes such as e.g. weak appearing squeegee strokes might be overlooked. Therefore, proper sample alignment must be ensured prior to inspection. In addition, attention must be given to the presence of contamination such as dust in the inspection environment to avoid potential false alarms. The possible in-line integration of the inspection system into a closed manufacturing cycle is part of further research work.

It can be highlighted that the evaluation of methods to be capable for industry applications is highly dependent on the experimental design. This includes proper dataset generation mimicking the imbalanced inspection scenario as well as choosing suitable performance metrics. The choice of demanded recall and precision is dependent on the quality requirements of the application as well as on the method itself, e.g. patch-wise processing. Enabling demanded defect detection perfor-

1264 mance among required inspection speeds is challeng-  
 1265 ing, thus further research has to be conducted regarding  
 1266 industry applicable defect detection methods. Due to  
 1267 fast emerging unsupervised anomaly detection methods  
 1268 as listed in [33,34,35,41,44], it is planned to investigate  
 1269 their capability of defect detection on these challenging  
 1270 structured patterns in future research.

## 1271 Acknowledgments

1272 The research work was performed within the COMET  
 1273 -project “Deep on-line learning for highly adapt-  
 1274 able polymer surface inspection systems” (project-no.:  
 1275 879785) at the Polymer Competence Center Leoben  
 1276 GmbH (PCCL, Austria) within the framework of the  
 1277 COMET-program of the Federal Ministry for Climate  
 1278 Action, Environment, Energy, Mobility, Innovation and  
 1279 Technology and the Federal Ministry for Digital and  
 1280 Economic Affairs and with contributions by Burg De-  
 1281 sign GmbH. The PCCL is funded by the Austrian Gov-  
 1282 ernment and the State Governments of Styria, Lower  
 1283 Austria and Upper Austria.

## 1284 References

- 1285 [1] See JE, Drury CG, Speed A, Williams A, Khalandi N. The  
 1286 Role of Visual Inspection in the 21st Century. Proceed-  
 1287 ings of the Human Factors and Ergonomics Society Annual  
 1288 Meeting. 2017; 61(1): 262-6. Available from: doi: 10.1177/  
 1289 1541931213601548.
- 1290 [2] Peres RS, Jia X, Lee J, Sun K, Colombo AW, Barata J. Indus-  
 1291 trial Artificial Intelligence in Industry 4.0 – Systematic Review,  
 1292 Challenges and Outlook. IEEE Access. 2020; 8: 220121-39.
- 1293 [3] Aminabadi SS, Tabatabai P, Steiner A, Gruber DP, Friesen-  
 1294 bichler W, Habersohn C, et al. Industry 4.0 In-Line AI Quality  
 1295 Control of Plastic Injection Molded Parts. Polymers. 2022;  
 1296 14(17).
- 1297 [4] Javaid M, Haleem A, Singh RP, Rab S, Suman R. Exploring  
 1298 impact and features of machine vision for progressive industry  
 1299 4.0 culture. Sensors International. 2022; 3: 100132.
- 1300 [5] Ruiz L, González J, Cavas F. Improving the competitiveness of  
 1301 aircraft manufacturing automated processes by a deep neural  
 1302 network. Integrated Computer-Aided Engineering. 2023 05;  
 1303 30: 1-12.
- 1304 [6] Chin RT, Harlow CA. Automated Visual Inspection: A Survey.  
 1305 IEEE Transactions on Pattern Analysis and Machine Intelli-  
 1306 gence. 1982; PAMI-4(6): 557-73.
- 1307 [7] Ren Z, Fang F, Yan N, Wu Y. State of the Art in Defect  
 1308 Detection Based on Machine Vision. International Journal of  
 1309 Precision Engineering and Manufacturing-Green Technology.  
 1310 2022; 9(2): 661-91.
- 1311 [8] Silva RL, Rudek M, Szejka AL, Junior OC. Machine Vision  
 1312 Systems for Industrial Quality Control Inspections. In: Chi-  
 1313 abert P, Bouras A, Noël F, Ríos J, editors. Product Lifecycle  
 1314 Management to Support Industry 4.0 Cham: Springer Interna-  
 1315 tional Publishing; 2018. pp. 631-41.
- [9] Ebayyeh AARMA, Mousavi A. A Review and Analysis of 1316  
 Automatic Optical Inspection and Quality Monitoring Methods 1317  
 in Electronics Industry. IEEE Access. 2020; 8: 183192-271. 1318
- [10] Huang SH, Pan YC. Automated visual inspection in the semi- 1319  
 conductor industry: A survey. Computers in Industry. 2015; 66: 1320  
 1-10. Available from: [https://www.sciencedirect.com/science/](https://www.sciencedirect.com/science/article/pii/S0166361514001845) 1321  
[article/pii/S0166361514001845](https://www.sciencedirect.com/science/article/pii/S0166361514001845). 1322
- [11] Kumar A. Computer-Vision-Based Fabric Defect Detection: 1323  
 A Survey. IEEE Transactions on Industrial Electronics. 2008; 1324  
 55(1): 348-63. 1325
- [12] Hanbay K, Talu MF, Özgüven ÖF. Fabric defect detection 1326  
 systems and methods – A systematic literature review. Opt- 1327  
 tik. 2016; 127(24): 11960-73. Available from: [https://www.](https://www.sciencedirect.com/science/article/pii/S0030402616311366) 1328  
[sciencedirect.com/science/article/pii/S0030402616311366](https://www.sciencedirect.com/science/article/pii/S0030402616311366). 1329
- [13] Kuo CFJ, Wang WR, Barman J. Automated Optical Inspec- 1330  
 tion for Defect Identification and Classification in Actual Wo- 1331  
 ven Fabric Production Lines. Sensors. 2022; 22(19): 7246. 1332  
 Available from: <https://www.mdpi.com/1424-8220/22/19/7246>. 1333
- [14] Vans M, Schein S, Staelin C, Kisilev P, Simske S, Dagan R, et 1334  
 al. Automatic visual inspection and defect detection on vari- 1335  
 able data prints. Journal of Electronic Imaging. 2011; 20(1): 1336  
 013010-0. 1337
- [15] Zhang E, Chen Y, Gao M, Duan J, Jing C. Automatic Defect 1338  
 Detection for Web Offset Printing Based on Machine Vision. 1339  
 Applied Sciences. 2019; 9(17): 3598. Available from: [https://](https://www.mdpi.com/2076-3417/9/17/3598) 1340  
[www.mdpi.com/2076-3417/9/17/3598](https://www.mdpi.com/2076-3417/9/17/3598). 1341
- [16] Sun N, Cao B. Real-Time Image Defect Detection System of 1342  
 Cloth Digital Printing Machine. Computational Intelligence 1343  
 and Neuroscience. 2022; 2022: 5625945. Available from: [https](https://www.hindawi.com/journals/cin/2022/5625945/) 1344  
[://www.hindawi.com/journals/cin/2022/5625945/](https://www.hindawi.com/journals/cin/2022/5625945/). 1345
- [17] Hachem CE, Perrot G, Painvin L, Couturier R. Automation 1346  
 of Quality Control in the Automotive Industry Using Deep 1347  
 Learning Algorithms. In: 2021 International Conference on 1348  
 Computer, Control and Robotics (ICCCR); 2021. pp. 123-7. 1349
- [18] Zhou Q, Chen R, Huang B, Liu C, Yu J, Yu X. An Automatic 1350  
 Surface Defect Inspection System for Automobiles Using Ma- 1351  
 chine Vision Methods. Sensors. 2019; 19(3): 644. Available 1352  
 from: <https://www.mdpi.com/1424-8220/19/3/644>. 1353
- [19] Gruber DP, Macher J, Haba D, Berger GR, Pacher G, Friesen- 1354  
 bichler W. Measurement of the visual perceptibility of sink 1355  
 marks on injection molding parts by a new fast processing 1356  
 model. Polymer Testing. 2014; 33: 7-12. 1357
- [20] Gospodnetić P, Hirschenberger F. Detection and Visibility Es- 1358  
 timation of Surface Defects Under Various Illumination Angles 1359  
 Using Bidirectional Distribution Function and Local Binary 1360  
 Pattern. In: Lončarić S, Cupec R, editors. Proceedings of the 1361  
 Croatian Computer Vision Workshop, Year 4. Center of Excel- 1362  
 lence for Computer Vision. Osijek: University of Zagreb; 2016. 1363  
 pp. 9-14. Available from: doi: 10.20532/ccvw.2016.0002. 1364
- [21] Lin HI, Wibowo FS. Image Data Assessment Approach for 1365  
 Deep Learning-Based Metal Surface Defect-Detection Sys- 1366  
 tems. IEEE Access. 2021; 9: 47621-38. 1367
- [22] Ultraviolet (UV) Image Sensor | Products & Solutions | Sony 1368  
 Semiconductor Solutions Group [homepage on the Inter- 1369  
 net]; cited 2024-05-28. Available from: [https://www.sony-](https://www.sony-semicon.com/en/products/is/industry/uv.html) 1370  
[semicon.com/en/products/is/industry/uv.html](https://www.sony-semicon.com/en/products/is/industry/uv.html). 1371
- [23] Hashagen J. Seeing Beyond the Visible. Optik & Photonik. 1372  
 2015; 10(3): 34-7. 1373
- [24] Amigo JM, Grassi S. Configuration of hyperspectral and mul- 1374  
 tispectral imaging systems. In: Hyperspectral Imaging. vol. 32 1375  
 of Data Handling in Science and Technology. Elsevier; 2019. 1376  
 pp. 17-34. 1377
- [25] Feng CH, Makino Y, Oshita S, García Martín JF. Hyperspec- 1378  
 tral imaging and multispectral imaging as the novel techniques 1379

- for detecting defects in raw and processed meat products: Current state-of-the-art research advances. *Food Control*. 2018; 84: 165-76.
- [26] Calvini R, Ulrici A, Amigo JM. Growing applications of hyperspectral and multispectral imaging. In: *Hyperspectral Imaging*. vol. 32 of *Data Handling in Science and Technology*. Elsevier; 2019. pp. 605-29.
- [27] Serranti S, Bonifazi G. Hyperspectral imaging and its applications. In: Berghmans F, Mignani AG, editors. *Optical Sensing and Detection IV*. SPIE Proceedings. SPIE; 2016; p. 98990P.
- [28] Prunella M, Scardigno RM, Buongiorno D, Brunetti A, Longo N, Carli R, et al. Deep Learning for Automatic Vision-Based Recognition of Industrial Surface Defects: A Survey. *IEEE Access*. 2023; 11: 43370-423.
- [29] Qi S, Yang J, Zhong Z. A Review on Industrial Surface Defect Detection Based on Deep Learning Technology. In: *2020 The 3rd International Conference on Machine Learning and Machine Intelligence*. New York, NY, USA: ACM; 2020. pp. 24-30.
- [30] Jin Q, Chen L. A survey of surface defect detection of industrial products based on a small number of labeled data. *arXiv preprint arXiv:220305733*. 2022. Available from: doi: 10.48550/arXiv.2203.05733.
- [31] Bergmann P, Batzner K, Fauser M, Sattlegger D, Steger C. The MVTEC Anomaly Detection Dataset: A Comprehensive Real-World Dataset for Unsupervised Anomaly Detection. *International Journal of Computer Vision*. 2021; 129(4): 1038-59.
- [32] Roth K, Pemula L, Zepeda J, Scholkopf B, Brox T, Gehler P. Towards Total Recall in Industrial Anomaly Detection. In: *2022 IEEE/CVF Conference on Computer Vision and Pattern Recognition (CVPR)*. IEEE Computer Society; 6/18/2022-6/24/2022. pp. 14298-308.
- [33] Xie G, Wang J, Liu J, Zheng F, Jin Y. Pushing the Limits of Fewshot Anomaly Detection in Industry Vision: Graphcore. *arXiv e-prints*. 2023. Available from: <http://arxiv.org/pdf/2301.12082.pdf>.
- [34] Li H, Hu J, Li B, Chen H, Zheng Y, Shen C. Target before Shooting: Accurate Anomaly Detection and Localization under One Millisecond via Cascade Patch Retrieval. *arXiv e-prints*. 2023. Available from: <https://arxiv.org/pdf/2308.06748v1.pdf>.
- [35] Batzner K, Heckler L, König R. EfficientAD: Accurate Visual Anomaly Detection at Millisecond-Level Latencies. *arXiv e-prints*. 2023. Available from: <http://arxiv.org/pdf/2303.14535.pdf>.
- [36] Bergmann P, Löwe S, Fauser M, Sattlegger D, Steger C. Improving Unsupervised Defect Segmentation by Applying Structural Similarity to Autoencoders. 2019; 372-80. Available from: <http://arxiv.org/pdf/1807.02011v3>.
- [37] Zavrtnik V, Kristan M, Skočaj D. DRAEM – A Discriminatively Trained Reconstruction Embedding for Surface Anomaly Detection. In: *Proceedings of the IEEE/CVF International Conference on Computer Vision (ICCV)*; 2021; pp. 8330-9.
- [38] Schlegl T, Seeböck P, Waldstein SM, Schmidt-Erfurth U, Langs G. Unsupervised anomaly detection with generative adversarial networks to guide marker discovery. In: *International conference on information processing in medical imaging*. Springer; 2017; pp. 146-57.
- [39] Zhang L, Dai Y, Fan F, He C. Anomaly Detection of GAN Industrial Image Based on Attention Feature Fusion. *Sensors (Basel, Switzerland)*. 2022; 23(1).
- [40] Zhang H, Wang Z, Wu Z, Jiang YG. Diffusionad: Denoising diffusion for anomaly detection. *arXiv preprint arXiv:230308730*. 2023. Available from: doi: 10.48550/arXiv.2303.08730.
- [41] Mousakhan A, Brox T, Tayyub J. Anomaly Detection with Conditioned Denoising Diffusion Models. *arXiv e-prints*. 2023. Available from: <https://arxiv.org/pdf/2305.15956.pdf>.
- [42] Tebbe J, Tayyub J. D3AD: Dynamic Denoising Diffusion Probabilistic Model for Anomaly Detection. *arXiv preprint arXiv:240104463*. 2024. Available from: doi: 10.48550/arXiv.2401.04463.
- [43] Yu J, Zheng Y, Wang X, Li W, Wu Y, Zhao R, et al. FastFlow: Unsupervised Anomaly Detection and Localization via 2D Normalizing Flows. *arXiv e-prints*. 2021. Available from: <http://arxiv.org/pdf/2111.07677.pdf>.
- [44] Zhou Y, Xu X, Song J, Shen F, Shen HT. MSFlow: Multi-Scale Flow-based Framework for Unsupervised Anomaly Detection. *arXiv e-prints*. 2023. Available from: <https://arxiv.org/pdf/2308.15300v1.pdf>.
- [45] Deng J, Dong W, Socher R, Li LJ, Li K, Fei-Fei L. Imagenet: A large-scale hierarchical image database. In: *2009 IEEE conference on computer vision and pattern recognition*. IEEE; 2009. pp. 248-55.
- [46] Goodfellow I, Pouget-Abadie J, Mirza M, Xu B, Warde-Farley D, Ozair S, et al. Generative adversarial nets. *Advances in Neural Information Processing Systems*. 2014; 27.
- [47] Li CL, Sohn K, Yoon J, Pfister T. Cutpaste: Self-supervised learning for anomaly detection and localization. In: *Proceedings of the IEEE/CVF conference on computer vision and pattern recognition*; 2021; pp. 9664-74.
- [48] Haselmann M, Gruber D. Supervised Machine Learning Based Surface Inspection by Synthetizing Artificial Defects. In: *International Conference on Machine Learning and Applications Cancun Mt, editor. ICMLA 2017: proceedings 16th IEEE International Conference on Machine Learning and Applications: 18-21 December 2017, Cancun, Mexico*. IEEE; 2017. pp. 390-5.
- [49] Niu S, Li B, Wang X, Lin H. Defect Image Sample Generation With GAN for Improving Defect Recognition. *IEEE Transactions on Automation Science and Engineering*. 2020; 1-12.
- [50] He X, Luo Z, Li Q, Chen H, Li F. DG-GAN: A High Quality Defect Image Generation Method for Defect Detection. *Sensors (Basel, Switzerland)*. 2023; 23(13).
- [51] Zhong X, Zhu J, Liu W, Hu C, Deng Y, Wu Z. An Overview of Image Generation of Industrial Surface Defects. *Sensors*. 2023; 23(19): 8160.
- [52] Duan Y, Hong Y, Niu L, Zhang L. Few-shot defect image generation via defect-aware feature manipulation. In: *Proceedings of the AAAI Conference on Artificial Intelligence*. vol. 37; 2023. pp. 571-8.
- [53] Hu T, Zhang J, Yi R, Du Y, Chen X, Liu L, et al. Anomalydiffusion: Few-shot anomaly image generation with diffusion model. In: *Proceedings of the AAAI Conference on Artificial Intelligence*. vol. 38; 2024. pp. 8526-34.
- [54] Tai Y, Yang K, Peng T, Huang Z, Zhang Z. Defect Image Sample Generation With Diffusion Prior for Steel Surface Defect Recognition. *arXiv preprint arXiv:240501872*. 2024. Available from: doi: 10.48550/arXiv.2405.01872.
- [55] Capogrosso L, Girella F, Taioli F, Chiara M, Aqeel M, Fummi F, et al. Diffusion-Based Image Generation for In-Distribution Data Augmentation in Surface Defect Detection. In: *Proceedings of the 19th International Joint Conference on Computer Vision, Imaging and Computer Graphics Theory and Applications-(Volume 2)*. SciTePress; 2024. pp. 409-16.
- [56] Zhao Z, Li B, Liu T, Zhang S, Lu J, Geng L, et al. Visual inspection system for battery screen print using joint method

- with multi-level block matching and K nearest neighbor algorithm. *Optik*. 2022; 250: 168332. Available from: <https://www.sciencedirect.com/science/article/pii/S0030402621018453>.
- [57] Jiang J, Cao P, Lu Z, Lou W, Yang Y. Surface Defect Detection for Mobile Phone Back Glass Based on Symmetric Convolutional Neural Network Deep Learning. *Applied Sciences*. 2020; 10(10): 3621.
- [58] Yuan ZC, Zhang ZT, Su H, Zhang L, Shen F, Zhang F. Vision-Based Defect Detection for Mobile Phone Cover Glass using Deep Neural Networks. *International Journal of Precision Engineering and Manufacturing*. 2018; 19(6): 801-10.
- [59] Zhou Z, Rahman Siddiquee MM, Tajbakhsh N, Liang J. UNet++: A Nested U-Net Architecture for Medical Image Segmentation. In: *International Conference on Machine Learning and Applications Cancún Mt*, editor. *ICMLA 2017: proceedings 16th IEEE International Conference on Machine Learning and Applications: 18–21 December 2017, Cancun, Mexico*. IEEE; 2017. pp. 3-11. Available from: [https://link.springer.com/chapter/10.1007/978-3-030-00889-5\\_1](https://link.springer.com/chapter/10.1007/978-3-030-00889-5_1).
- [60] Yoon B, Lee H, Jeong J. Improved U-Net++ with Patch Split for Micro-Defect Inspection in Silk Screen Printing. *Applied Sciences*. 2022; 12(9): 4679.
- [61] Gafurov AN, Phung TH, Ryu BH, Kim I, Lee TM. AI-Aided Printed Line Smearing Analysis of the Roll-to-Roll Screen Printing Process for Printed Electronics. *International Journal of Precision Engineering and Manufacturing-Green Technology*. 2023; 10(2): 339-52.
- [62] Deltamax [homepage on the Internet]; cited 2024-02-07. Available from: <https://deltamaxe.com/en/products/glassinspector/>.
- [63] Elunic [homepage on the Internet]; cited 2024-02-07. Available from: <https://www.elunic.com/de/aisec/qualitaetssicherung-presswerk-ki/>.
- [64] Lake Image [homepage on the Internet]; cited 2024-02-07. Available from: <https://lakeimage.com/products/discovery-roll-inspector/>.
- [65] Nireco Corporation [homepage on the Internet]; cited 2024-02-07. Available from: <https://nirecocom/en/product/surface-inspection/mujiken-plus.html>.
- [66] Solomon [homepage on the Internet]. cited 2024-02-07. Available from: <https://www.solomon-3d.com/solomon-vision>.
- [67] Stoba [homepage on the Internet]; cited 2024-02-07. Available from: <https://www.stoba.one/en/customized-machinery/technologies/visual-inspection>.
- [68] Dr. Schenk GmbH [homepage on the Internet]; cited 2024-02-07. Available from: <https://www.dr-schenk.com/products.html>.
- [69] ColorBrain [homepage on the Internet]; cited 2024-02-07. Available from: <https://www.baumerinspection.com/us/en/baumer-inspection-navigation/products/colourbrain-decoin-spector/a/decoinspector>.
- [70] In-Core Systemes [homepage on the Internet]; cited 2024-02-07. Available from: <https://www.in-core-systemes.com/compo-sites-materials/>.
- [71] Omso [homepage on the Internet]; cited 2024-02-07. Available from: <https://www.omso.it/en/p/ecolin>.
- [72] Cugher [homepage on the Internet]. cited 2024-02-07. Available from: <https://www.cugher.com/increased-quality-control-and-production-monitoring-for-industry-4-0>.
- [73] Keko Equipment [homepage on the Internet]; cited 2024-02-07. Available from: <https://www.keko-equipment.com/Inspection.php>.
- [74] Sakurai Graphic Systems Corporation [homepage on the Internet]; cited 2024-02-07. Available from: <https://www.sakurai-gs.co.jp/en/products/process/si.html>.
- [75] Krassnig PJ, Haselmann M, Gruber DP. Inspection Approach for Automated In-line Defect Detection on Decorated Foil Plates. *Advances in Signal Processing and Artificial Intelligence: Proceedings of the 4th International Conference on Advances in Signal Processing and Artificial Intelligence 19–21 October 2022 Corfu, Greece*. 2022: 84-5.
- [76] Biegeleisen JI. *Complete Book of Silk Screen Printing Production*. Dover Publications; 2012; Available from: <https://books.google.at/books?id=o8sKJSHeU-MC>.
- [77] Sauer M, Meilchen S, Kalleder A, Mennig M, Schmidt H. Screen Printing. In: Aegerter MA, editor. *Sol gel technologies for glass producers and users*. New York, NY: Springer Science + Business Media; 2011; pp. 117-22. Available from: [https://link.springer.com/chapter/10.1007/978-0-387-88953-5\\_14](https://link.springer.com/chapter/10.1007/978-0-387-88953-5_14).
- [78] *Handbook for screen printers*. Thal, Switzerland: Sefar; 2006.
- [79] ISO 12233:2000(en) [homepage on the Internet]; cited 2024-02-07. Available from: <https://www.iso.org/obp/ui>.
- [80] Haixiang G, Yijing L, Shang J, Mingyun G, Yuanyue H, Bing G. Learning from class-imbalanced data: Review of methods and applications. *Expert Systems with Applications*. 2017; 73: 220-39. Available from: <https://www.sciencedirect.com/science/article/pii/S0957417416307175>.
- [81] He H, Garcia EA. Learning from Imbalanced Data. *IEEE Transactions on Knowledge and Data Engineering*. 2009; 21(9): 1263-84.
- [82] Hambardzumyan S, Tuli A, Ghukasyan L, Rahman F, Topchyan H, Isayan D, et al. Deep Lake: a Lakehouse for Deep Learning. *arXiv e-prints*. 2022arXiv:2209.10785.
- [83] He K, Zhang X, Ren S, Sun J. Deep Residual Learning for Image Recognition. In: *Proceedings of the IEEE Conference on Computer Vision and Pattern Recognition (CVPR)*; 2016.
- [84] Loshchilov I, Hutter F. SGDR: Stochastic Gradient Descent with Warm Restarts. *arXiv e-prints*. 2016. Available from: <http://arxiv.org/pdf/1608.03983.pdf>.
- [85] Zagoruyko S, Komodakis N. Wide Residual Networks. *arXiv e-prints*. 2016. Available from: <http://arxiv.org/pdf/1605.07146.pdf>.
- [86] Johnson J, Douze M, Jegou H. Billion-Scale Similarity Search with GPUs. *IEEE Transactions on Big Data*. 2021; 7(3): 535-47.
- [87] Chicco D, Jurman G. The Matthews correlation coefficient (MCC) should replace the ROC AUC as the standard metric for assessing binary classification. *BioData Mining*. 2023; 16(1): 4. Available from: <https://biodatamining.biomedcentral.com/articles/10.1186/s13040-023-00322-4>.
- [88] Event – PyTorch 2.1. documentation [homepage on the Internet]; cited 2024-02-07. Available from: <https://pytorch.org/docs/stable/generated/torch.cuda.Event.html>.
- [89] Bianco S, Cadene R, Celona L, Napoletano P. Benchmark Analysis of Representative Deep Neural Network Architectures. *IEEE Access*. 2018; 6: 64270-7.
- [90] Haselmann M, Krassnig PJ, Gruber DP. Visual inspection of patterned surfaces with supervised deep learning using both real and synthetic defects. *Advances in Signal Processing and Artificial Intelligence: Proceedings of the 4th International Conference on Advances in Signal Processing and Artificial Intelligence 19–21 October 2022 Corfu, Greece*. 2022: 138-9.